We are IntechOpen, the world's leading publisher of Open Access books Built by scientists, for scientists

6,900
Open access books available

185,000
International authors and editors

200M
Downloads

Our authors are among the

154
Countries delivered to

TOP 1%
most cited scientists

12.2%
Contributors from top 500 universities



WEB OF SCIENCE™

Selection of our books indexed in the Book Citation Index in Web of Science™ Core Collection (BKCI)

Interested in publishing with us?
Contact book.department@intechopen.com

Numbers displayed above are based on latest data collected.
For more information visit www.intechopen.com



Chapter

Experimental Studies of and Theoretical Models for Detachment in Helical Fusion Devices

Masahiro Kobayashi and Mikhail Tokar

Abstract

Good plasma performance in magnetic fusion devices of different types, both tokamaks and helical devices, is achieved normally if the plasma density does not exceed a certain limit. In devices with a divertor, such as tokamaks JET, JT-60U, and heliotron large helical device (LHD), by approaching the density limit, the plasma detaches from the divertor target plates so that the particle and heat fluxes onto the targets reduce dramatically. This is an attractive scenario for fusion reactors, offering a solution to the plasma-wall interaction problem. However, the main concerns by realizing such a scenario are the stability of the detached zone. The activity on the heliotron LHD aimed on detachment stabilization, by applying a resonant magnetic perturbation (RMP) and generating a wide magnetic island at the plasma edge, will be reviewed. Also, theoretical models, explaining the detachment conditions, low-frequency oscillations at the detachment onset, and mechanisms of the detached plasma stabilization by RMP, will be discussed.

Keywords: helical device, LHD, detachment, resonant magnetic perturbation, nonlinear oscillations, modeling

1. Introduction

Handling of power loads onto divertor target plates is one of the most critical problems by the realization of a nuclear fusion reactor. The divertor configuration foreseen for ITER (International Thermonuclear Experimental Reactor) has been designed on the basis of present knowledge on physics and is currently available through most advanced engineering technology. It is presumed to handle a total heat load up to 100 MW, which is, however, expected to be reached during the DT (Deuterium-Tritium) plasma phase [1]. In devices beyond ITER, for example, DEMO (Demonstration Power Station), even much higher heat fluxes into the divertor volume are expected. Therefore, up to 90% of power, coming out of the confinement region, has to be removed before the plasma contacts the divertor plates to guarantee a long enough lifetime of the targets [2]. One of the most attractive ways to reach this is the realization of the state where the plasma is detached from the plates, and the energy is mostly dissipated through the radiation from impure particles in the whole divertor volume. The understanding of the detachment mechanisms and searching

IntechOpen

for possibilities to reliably control the strongly radiating divertor plasma, being simultaneously compatible with the confinement requirements for the plasma core, is one of the most important issues for fusion studies.

Although axis-symmetric tokamaks are presently the most advanced concept for the realization of the magnetic fusion, studies of the detachment in helical devices [3, 4] are also of high interest and importance for the reactor design. Because of inherently nonaxisymmetric magnetic configurations, the magnetic field topology in heliotrons has unique features, in particular, the existence of magnetic islands and stochasticity of field lines. The magnetic field in helical systems is completely generated by currents in external coils. Therefore, the field topology and its effects on the plasma transport and, in particular, on the plasma detachment conditions and characteristics can be studied by varying the magnetic structure in a wide range. Moreover, such investigations are also useful for tokamak devices, where recently resonant magnetic perturbations (RMP) have been introduced to mitigate excessive divertor power load [5, 6]. Due to RMP, the magnetic field in tokamaks exhibits similar structure as in helical devices, that is, with the presence of magnetic islands and stochastic field lines. Thus, the understanding of detachment features in heliotrons is, therefore, of general interest for magnetic fusion program.

The structure of the present chapter is as follows. In next section, we briefly review the features and main differences in the detachment phenomena in tokamaks and helical devices. Experimental observations on the detached divertor plasmas in LHD without and with the application of RMP are presented. The RMP generates a broad magnetic island embedded in the intrinsic edge stochastic layer, which significantly influences features such as the impurity radiation, divertor foot prints, and detachment stability. The impacts on the core plasma transport characteristics during the detached discharge phase are also analyzed here. In Section 3, an interpretation of the detachment phenomena and features of detached plasmas based on the edge plasma energy balance is presented. In Section 4, different mechanisms of nonlinear oscillations during the detachment onset both in helical devices and in tokamaks are discussed. Conclusions are summarized in Section 5.

2. Experimental observations on detachment in the heliotron LHD and comparison with tokamaks

2.1 Main characteristics of divertor plasmas

By rising the plasma density in tokamaks, the plasma in the scrape-off layer (SOL) and divertor goes through several qualitatively different "regimes" [7]. At a low density level, neutral particles, appearing by the recombination of electrons and ions on the divertor target plates, escape freely into the confined plasma volume. Here, these so-called recycling neutrals are ionized and charged species generated diffuse across the magnetic field back into the SOL. Such a particle convection effectively transports heat coming from the plasma core, and the temperatures of the plasma components vary weakly along the magnetic field in the SOL. This regime is referred as either the sheath-limited one or as that of a weak recycling.

With the increasing plasma density, the fraction of recycling neutrals ionized in the vicinity of the targets is growing up. Therefore, beyond the recycling zone, the plasma convection becomes relatively weaker. As a result, a significant parallel temperature gradient develops in the main part of the SOL and the energy toward the targets is transported predominantly by the heat conduction. This regime is called as the conduction limited or a high recycling one. On the one hand, due to the strong temperature dependence of the parallel heat conductivity, $T^{2.5}$, the temperature in

the SOL changes weakly with parameters such as the plasma density at the separatrix, n_s, being comparable with the density in the confined plasma, and the heat flux from the core. On the other hand, the plasma density near the divertor targets, n_t, and the plasma flux to the targets, Γ_t, rise rapidly with n_s, as $n_t\ n_s^3$ and $\Gamma_t\ n_s^2$, respectively [8]. As a result, the divertor plasma can be brought into a state of a very high density of $10^{20–21}$ m^{-3} and a temperature below 5 eV. Under these conditions, the impurity radiation plays an important role in the divertor power balance.

Contrarily to tokamaks in helical devices, such as LHD and W7-AS, it has been found that the SOL and divertor plasma characteristics do not show such strong nonlinear variation with n_s, even if this is already close to the threshold at the detachment onset, $n_t\ n_s^{1\sim1.5}$ [9, 10]. It has been interpreted as a result of the momentum (pressure) loss in the stochastic field line region [11, 12] or in the island divertor structure [10]. In these regions, parallel plasma particle flows, along flux tubes of very different connection lengths or even streaming in opposite directions [13], are strongly interconnected through the cross-field momentum transfer. Therefore, the divertor plasma density remains relatively low, of 10^{19} m^{-3}, and the temperature relatively high, of 10 eV, till the detachment transition [9]. (Numerical simulations for W7-X [14] predict, however, a high recycling regime, due to the larger spatial separation of the counter-streaming flows in the larger island.)

Nonetheless, experimental observations demonstrate that in the LHD impurity, radiation plays an important role for the divertor plasma cooling, detachment onset, and stability conditions. Here, however, the main radiation source is not located in the divertor legs but in the stochastic layer. **Figure 1** shows the tomographic reconstruction of carbon impurity emission in the edge stochastic layer of LHD just before the detachment transition, as well as the magnetic field line connection length (L_C) [15]. Although, the emission of low charge state, CII (C^{1+}), is distributed along divertor leg and the very periphery of the stochastic layer, that from the higher charge state, CIV (C^{3+}), being the main radiating species [16], comes from the stochastic layer only.

In the LHD, studies on the divertor detachment are performed by seeding impurities deliberately [17–19] and by applying RMP from special coils [20–22]. In this chapter, we focus on the detachment with the RMP application, which is a unique feature of the LHD.

2.2 RMP impact on the edge impurity radiation and stability of detached plasma

The large helical device, LHD, is a heliotron-type fusion machine, in which the magnetic field is produced by superconducting coils with poloidal and toroidal

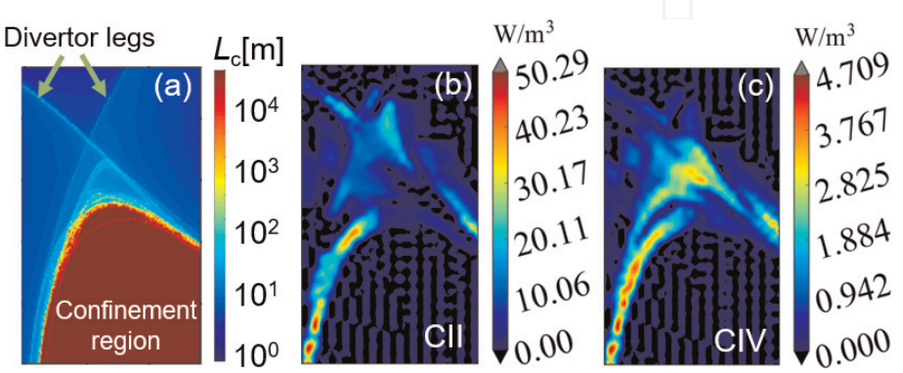


Figure 1.
The pattern of the connection length L_C in the edge stochastic layer of LHD (a); the tomographic reconstruction of the emission from carbon ions CII (514 nm) (b) and CIV (466 nm) (c), recorded just before the detachment onset, at line averaged plasma density $\overline{n}_e = 5 \times 10^{19}\ m^{-3}$.

winding numbers l = 2 and n = 10, respectively [23]. **Figure 2(b)** displays a poloidal cut of the calculated magnetic field structure in the edge region and the distribution of connection length L_C. The magnetic field in helical devices is completely generated by currents in external coils and has a broad spectrum of Fourier harmonics of different mode numbers m and n. Each of those generates magnetic islands, and by overlapping of the islands, the magnetic field structure becomes stochastic. The divertor legs, named left and right legs, are connected to the L and R divertor plates, respectively, rotating helically by moving in the toroidal direction. The lower half of the **Figure 2** presents the L_C distribution with RMP of m/n = 1/1, where the remnant island structure embedded into the stochastic layer is visible.

Figure 3 shows the time evolution of several plasma parameters in discharges with and without RMP where the density ramp up was performed without auxiliary impurity seeding, and the edge radiation was coming mainly from carbon impurity sputtered from the divertor target plates. On the one hand, without RMP (blue lines), the growth of the density leads to a sudden increase of the radiated power, see **Figure 3(b)**, and, finally, to the radiation collapse of the whole plasma. On the other hand, with the RMP application (red lines), the radiated power is saturated at a higher level and the state with the plasma detached from the divertor targets is sustained during the whole later phase of the discharge. This is demonstrated in **Figure 3(a)** by the evolution of the heat load onto the divertor target. The strong cooling of the edge plasma by impurity radiation leads to the decrease of the plasma column effective radius a_{99} displayed in **Figure 3(d)**.

Figure 4 shows the radial profiles of the electron temperature T_e, density n_e, and pressure in the edge region along the LHD mid-plane, in the attached and detached discharge phases [24]. With the RMP application, a clear flattening of the T_e profile due to the magnetic island is observed at the outboard, R = 4.60–4.75 m, in the attached phase. The increase in the density leads to the lowering of T_e, and during the detached phase, T_e inside the island is sustained at ~20 eV. It is also interesting to note that with the growing n_e, the width of the region with the profile flattening becomes slightly narrower, and at the same time, a region with the flattening appears

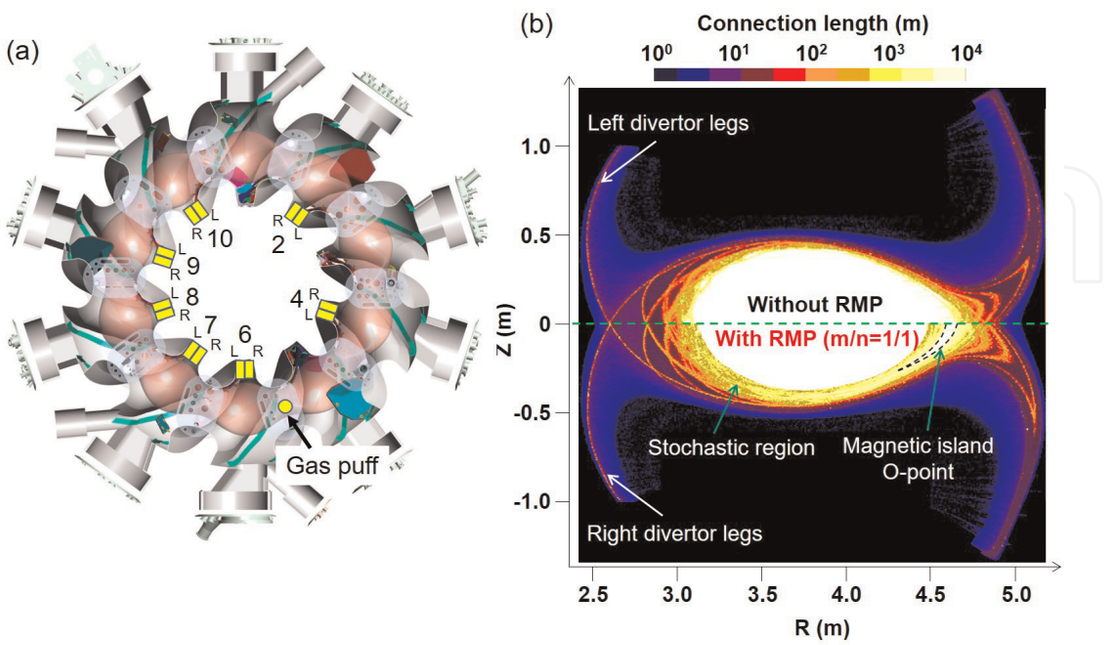


Figure 2.
Top view of the LHD torus with the position of divertor probe arrays at the inboard, indicated by numbers and letters "L"& "R" (a); L_C distribution in the edge region of LHD, without (upper half) and with (lower half) RMP application (b). The right and left legs, indicated in the figure, are connected to L and R divertor arrays, respectively.

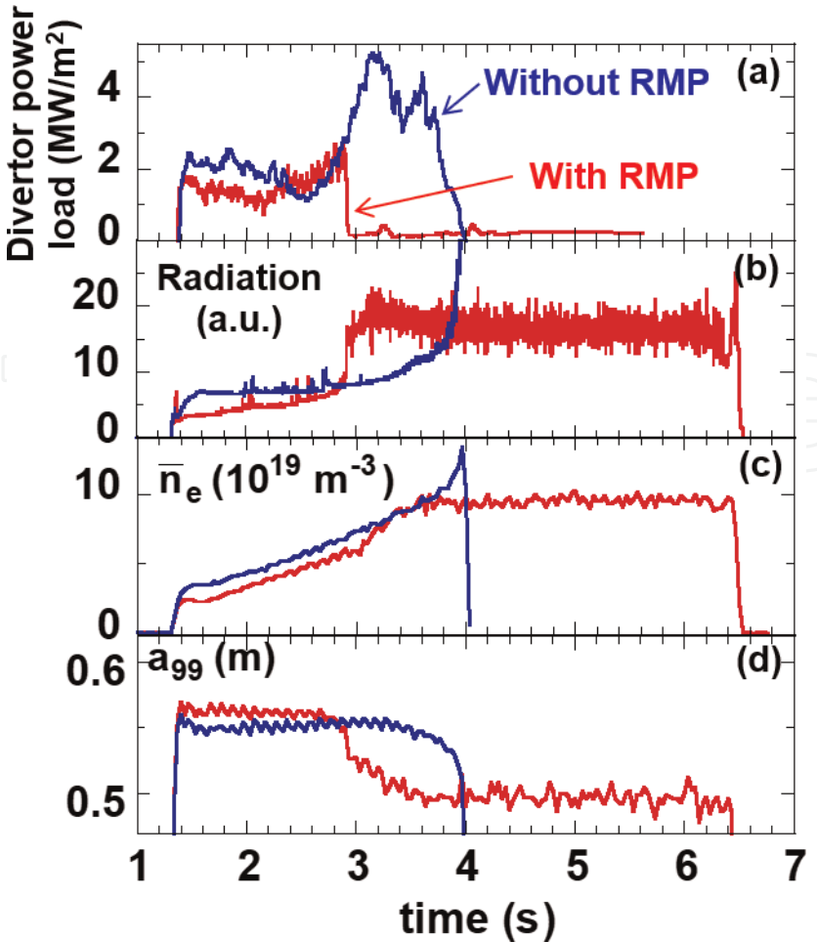


Figure 3.
Time evolution of plasma parameters in the LHD density ramp-up discharges, with (red) and without (blue) the RMP application: The power load onto divertor targets measured by probes (a), the radiated power measured by AXUV (b), line averaged density (c), and the effective plasma minor radius a_{99} defined as that of the flux surface, containing 99% of the total plasma energy (d).

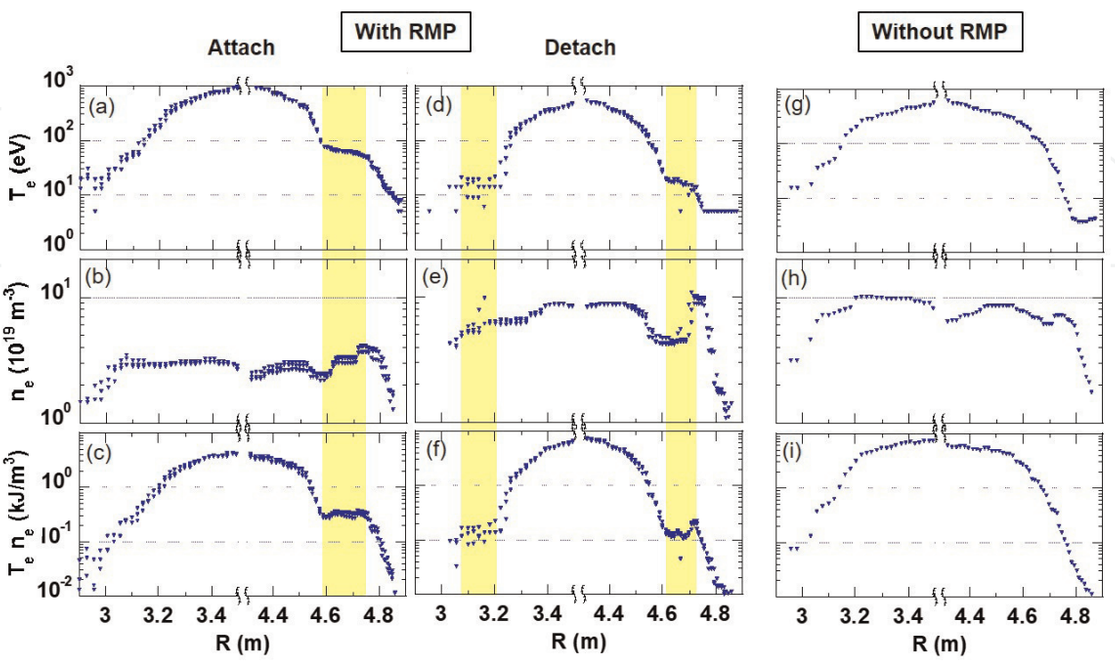


Figure 4.
Radial profiles of the plasma parameters in the LHD edge region: electron temperature (a, d, g), density (b, e, h), and pressure (c, f, i); the panels (a–f) correspond to discharges with RMP, (g–i)—without RMP. The region of the T_e flattening caused by the magnetic island is indicated by yellow patch [24].

at the inboard, R = 3.1–3.2 m. This is interpreted as a result of the plasma response to the external RMP field. Indeed, the measurements with a saddle loop coil indicate the reduction of the total field perturbation by RMP induced by the currents in the plasma under the attached conditions and its amplification during the detached phase [20, 25, 26]. A similar flattening appears in the pressure profiles, while density is relatively flat in the entire edge region with some modulations around the magnetic island. Without RMP application, there is no such flattening except for a small modulation due to the inherent small remnant islands of higher mode numbers.

The edge impurity radiation profiles are estimated using the T_e and n_e profiles presented in **Figure 4** and by assuming a concentration of carbon of 1% with respect to n_e. **Figure 5** shows the temporal evolution of the radiation profiles together with L_C distributions [24]. Without RMP, **Figure 5(b)**, the impurity radiation starts to peak around the X-point of the divertor leg, at R ~ 4.8 m, and later moves gradually radially inward due to the decrease in the temperature as the density increases; the X-point of the divertor leg should be distinguished from that of the magnetic island created by the RMP. Finally, the radiation penetrates into the confinement region at t = 4 sec, leading to the radiation collapse, as shown in **Figure 3**. With the RMP application, **Figure 5(a)**, a bundle of flux tubes of long connection length appears at the edge, as a remnant island. The radiation starts to peak at the X-point of the divertor leg and moves radially inward, similarly to the case without RMP. It is, however, stopped at the periphery of the edge of the island, R ~ 4.75 m, without penetrating into the confinement region at the detachment transition, t 2.9 sec. Then, the discharge is sustained until the end of NBI heating due to the stabilization of the radiation profile by the island.

Radiation profile measurements have been performed to capture the change of the global structure of impurity emission due to RMP and are compared with numerical transport simulations with the code EMC3-EIRENE [20–22]. **Figure 6** shows the calculated impurity radiation distribution, with and without RMP, and

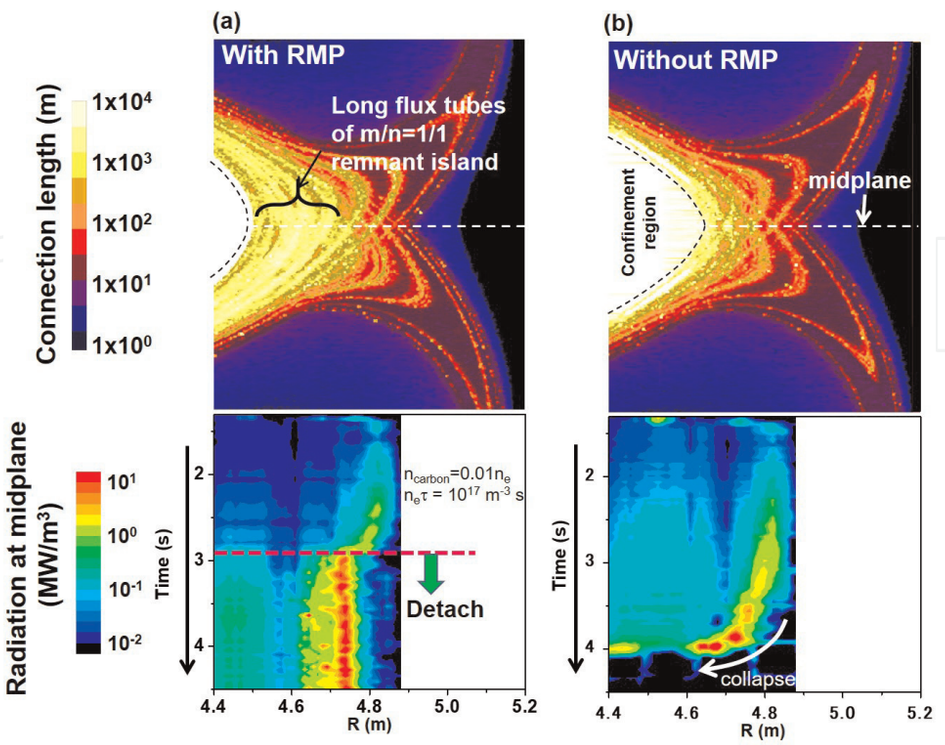


Figure 5.
The calculated L_C distribution in the outboard edge region (upper panels); time evolution of the carbon radiation estimated from T_e and n_e profiles as shown in **Figure 4**, *by assuming 1% carbon concentration and noncoronal cooling rate at $n_e\tau = 10^{17}$ m^{-3} s (lower panels), with (a) and without (b) RMP [24].*

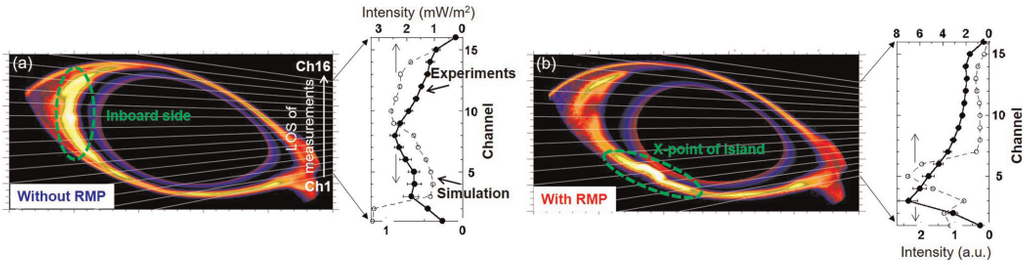


Figure 6.
Carbon impurity radiation distribution calculated by EMC3-EIRENE at poloidal cross section, together with line-integrated profile of the simulation and measurements by AXUV, on the right panel, without (a) and with (b) RMP [20].

the radiation profile measured by the AXUV diagnostics [20]. Without the RMP application, the impurity radiation is enhanced at the inboard as it is demonstrated in **Figure 6(a)**. The line integrated radiation profile found both in the measurements and in simulations are shown in the right panel. Both profiles have maxima at the center channels, which pass through the enhanced radiation at the inboard location. With the RMP, the peak of the radiation moves to the bottom of the plasma, where the X-point of the m/n = 1/1 island is located (note that the toroidal angle positions of the cross sections are different in **Figures 2(b)** and **6**). The simulation also shows a peak at the bottom channel in accordance with the measurement. The measurements by imaging bolometer also indicate enhanced radiation around X-point in agreement with the numerical simulation [21].

The impact of RMP on the impurity emission intensity was also investigated in the VUV range with the diagnostic equipment [22], viewing the entire plasma toroidal cross section. Density dependence of the radiated power measured by the resistive bolometer, together with emissions from different charge states, CIII (C^{2+}), CIV (C^{3+}), CV (C^{4+}), and CVI (C^{5+}), measured with the spectrometer [27] is plotted in **Figure 7**. Here, the plasma density is normalized to the density limit in helical devices, n_{sudo} [28]. It is seen that without RMP, the radiated power shows rapid increase around the density limit, that is, $\left.\frac{\partial P_{bolo}}{\partial n_e}\right|_{without\ RMP} \rightarrow$. This means that any small density perturbation leads to a significant change in the radiation; that is, the system in question is becoming unstable. With RMP, the radiation is enhanced in the low-density range even in the attached phase. The increase of the radiation with RMP is interpreted due to the enlarged volume inside the edge magnetic island with a low T_e, of 10–20 eV where the radiation of low charged carbon ions approaches its maximum. After the detachment transition, there appears a region where the radiation is insensitive to the density, that is, $\left.\frac{\partial P_{bolo}}{\partial n_e}\right|_{with\ RMP} \rightarrow \mathbf{0}$. This provides a possibility to the radiation level control and, thereby, the detachment stability. One can see that the "flat" region extends slightly beyond the density limit, which results in an extension of density operation range for the case with RMP. Very similar density dependence as for the bolometer measurement is observed in the emission of CIII and CIV species, being the dominant radiating charge states, see **Figure 7(b)** and **(c)**. As it is analyzed in Ref. [16], CIV is providing the largest contribution to the total radiated power. On contrary, with RMP, the radiation of CV and CVI ions increases monotonically with the plasma density, and is larger than without RMP. Since the ionization energies of CV and CVI ions, 392 and 490 eV, respectively, are much higher than the T_e inside the magnetic island, the higher emission intensity might indicate enhanced penetration of impurity toward the core boundary. The contribution of CV and CVI to the total radiated power is, however, small compared to the states of lower charges [16].

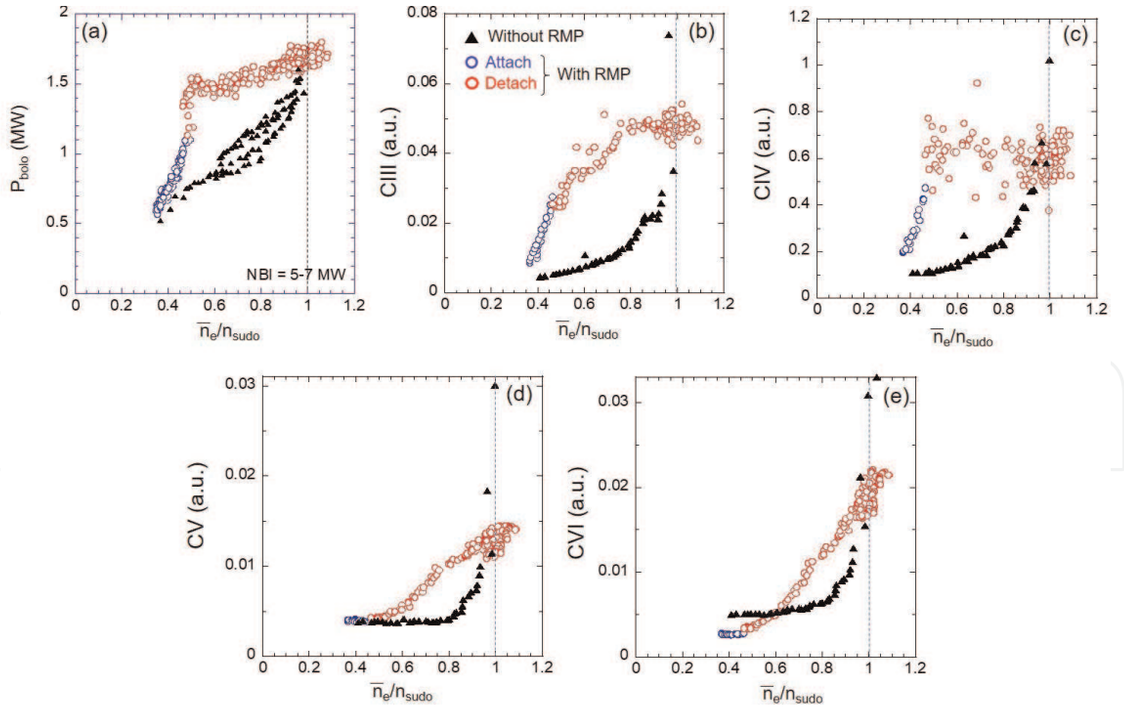


Figure 7.
Density dependence of the radiated power measured by the bolometer (a), the emissivity of CIII (b), CIV (c), CV (d), and CVI (e) species measured by VUV spectrometer without (triangles) and with (circles) RMP. The density is normalized to the density limit in helical devices, n_{sudo} [27].

The results above clearly show the difference of edge impurity radiation and transport with and without RMP. This is of high importance for the detachment stabilization in the former situation. The mechanism of the stabilization of the radiation layer is under investigation by taking into account the magnetic geometry, the particle, and the energy transport, both parallel and perpendicular to the field lines within and out of the magnetic island. Similar observations of the detached plasma stabilization with large island were also found in W7-AS [29]. The recent results on the successful detachment control in W7-X with the island divertor also suggest an important role of the edge magnetic island for the detached plasma stability [30].

2.3 Change of divertor footprint with RMP application

The toroidal variation of the particle fluxes onto divertor plates with RMP has been investigated with Langmuir probe array installed around the mid-plane of the targets at the inboard side [17, 31]. It has been found that the time evolution of the divertor particle flux exhibits substantial difference between toroidal locations, that is, some plates are becoming detached earlier than others; at some plates, the flux even increases after detachment [27]. The summary of this behavior is shown in **Figure 8**, where the divertor particle flux normalized to its value without RMP is plotted for different toroidal sections. In the attached case, there is an n = 1 mode structure for both left (L) and right (R) divertor arrays, which are connected to the left and right legs, respectively, as indicated in **Figure 2**. In the detached phase, the n = 1 structure remains, but the toroidal phase is shifted by one section. The relation between the divertor flux and L_C profiles is presented in **Figure 9** for several toroidal cross sections [27]. At the section 6L (**Figure 9(a)** and **(b)**), a bundle of flux tubes of 6.5 mm width is connected to the divertor plate. By applying RMP, the footprint shifts toward the right side with increased L_C. The measured particle flux increases in the absolute values due to the longer L_C, as seen also in **Figure 9(a)**.

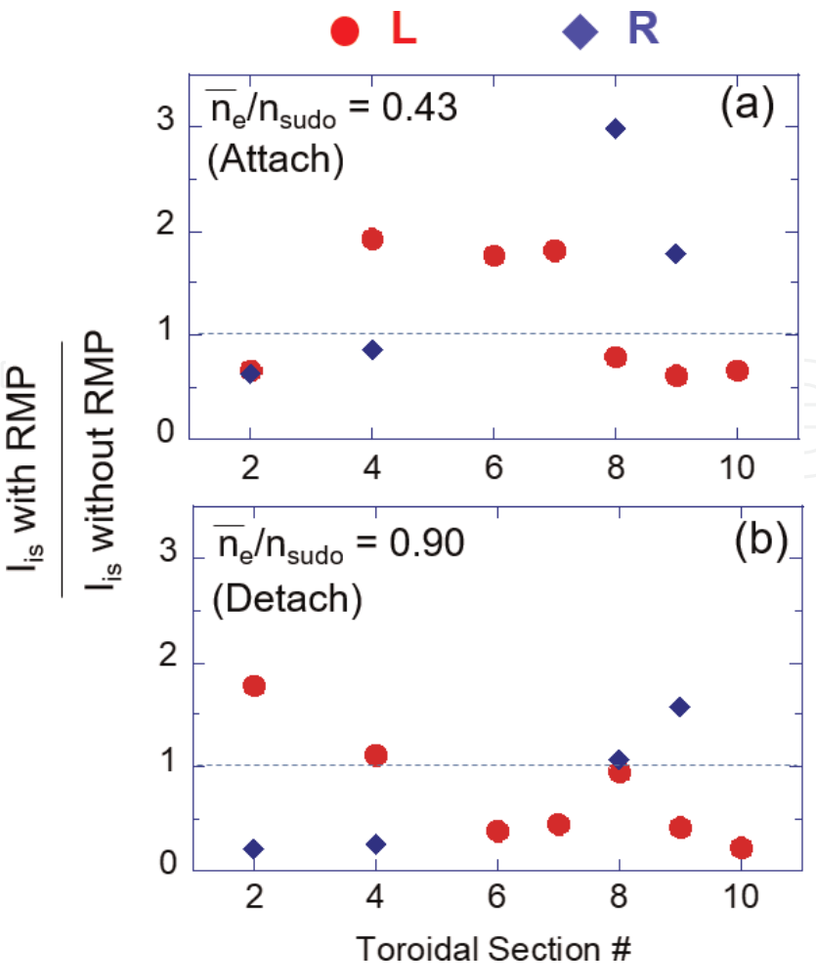


Figure 8.
The toroidal distributions of the particle flux onto divertor targets with RMP normalized by the values without RMP on attached (a) and detached (b) discharge phases. Red circles correspond to the left divertor and blue diamonds to the right divertor arrays, as it is indicated in **Figure 2** *by the toroidal section number [27].*

The flux profile becomes more asymmetric with respect to the central peak, being increased at the right side, which reflects the right shift of the L_C footprint. On the other hand, the 2R plate shows decrease of the particle flux with the RMP application, as seen in **Figure 9(c)**. This is interpreted by the decrease in L_C, as shown in the figure, where the long L_C bundle at the central region almost disappears with RMP, and thus, the particle flux decreases as well. These results show that, to a certain extent, the particle transport is well correlated with the L_C distribution calculated in the vacuum approximation, i.e., without a plasma response to RMP, and thus can be controlled by the RMP application in the attached phase. In the detached phase, the particle flux both at 6L and 2R decreases in the entire region with respect to the case without RMP, as shown in **Figure 9(b)** and **(d)**.

In **Figure 9(e)** and **(f)**, the observations in section 2L are presented. By applying RMP, the particle flux becomes smaller in the attached phase with respect to the reference case without RMP. The flux, however, increases at the detached phase, as shown in **Figure 9(f)**. At this plate, the fraction of long flux tubes with $L_C > 100$ m decreases, but those with $L_C \sim 30$ m increases with RMP. The reduction of the flux at the attached phase may be due to the reduction of the contribution from the tubes with $L_C > 100$ m. On the other hand, in the detached phase, the increases of the flux could be attributed to the change of the particle transport channel from long, $L_C > 100$ m, to the medium, $L_C \sim 30$ m, flux tubes. This effect has to be investigated by analyzing in detail the relation between the magnetic field structure and the ionization front. It has to be taken into account that there is a significant

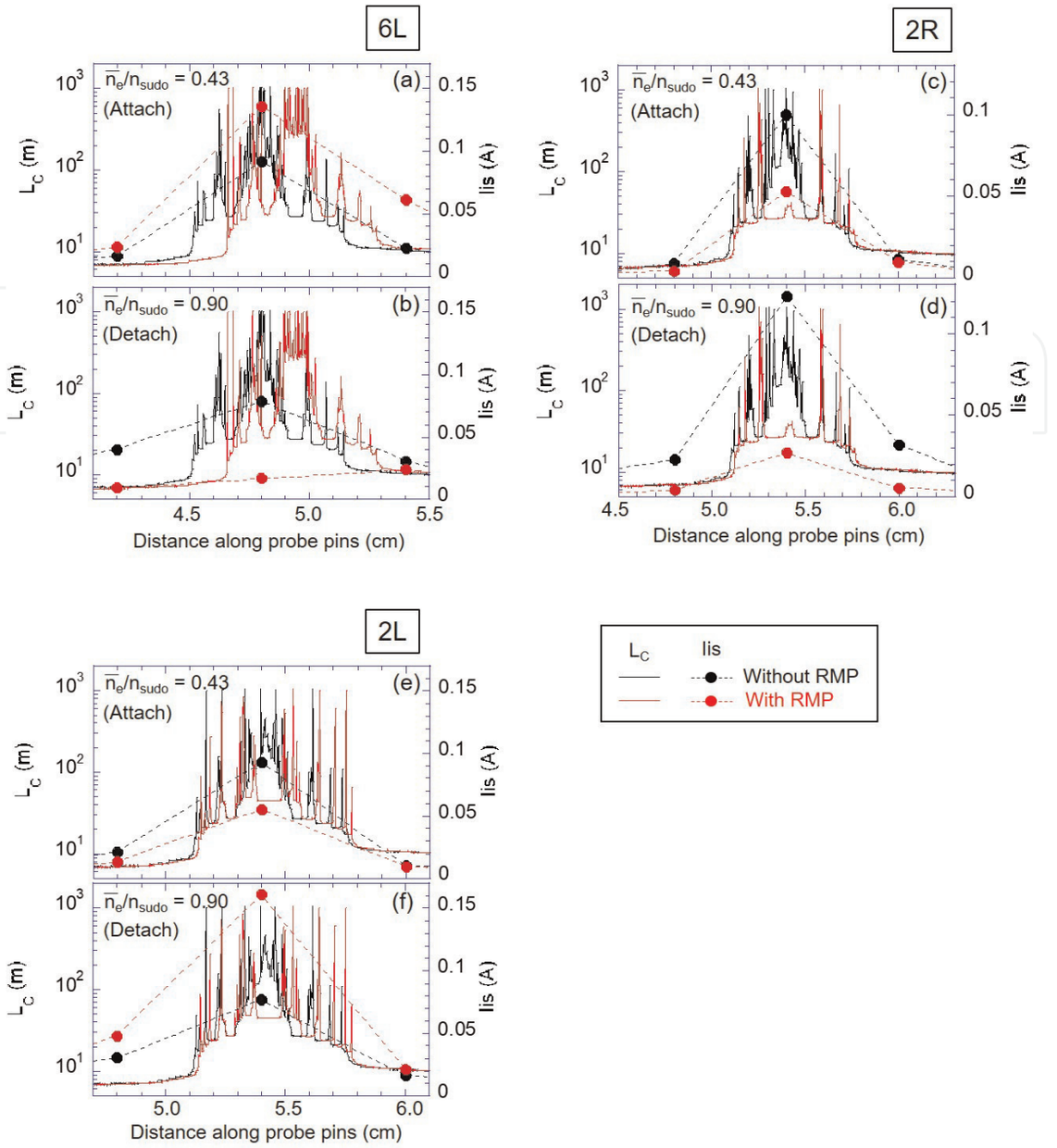


Figure 9.
L_C (solid lines) and divertor particle flux (dashed lines with circles) profiles along the divertor probe pins, with (red) and without (black) RMP. (a and b) 6L, (c and d) 2R, and (e and f) 2L toroidal section, respectively [27].

plasma response to the RMP, which is different in the attached and detached phases, as mentioned above.

During the detached phase, there are large oscillation in both divertor particle flux and radiation. **Figure 10** presents the time traces of the particle flux to the divertor targets and of the radiation losses measured by AXUV during the detached phase, where oscillation with 60–90 Hz is visible. The particle flux and radiation are oscillating in phase. Similar behavior was also observed in the particle flux to the first wall [32]. The mechanism of the oscillation is discussed later in this chapter.

2.4 Operation space of detachment: amplitude and radial location of resonance layer of RMP

The parameter space of a stable discharge performance with the RMP and the plasma detached from the divertor targets has been investigated by varying the

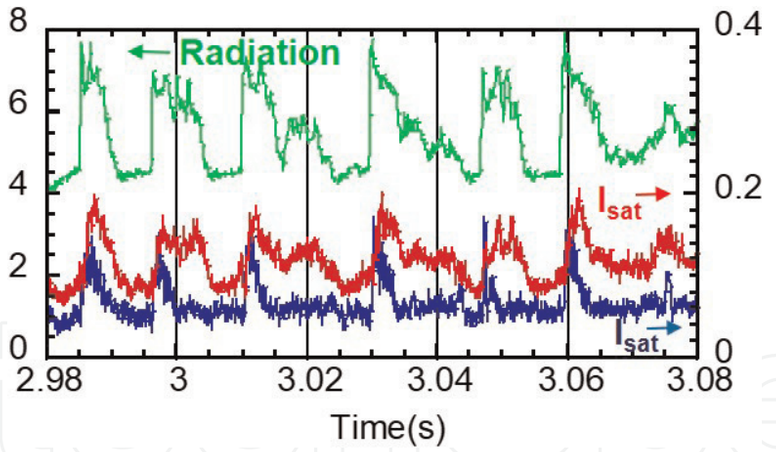


Figure 10.
Time traces of the radiation losses, measured by the AXUV (green line), and that of the particle flux to divertor targets (red and blue lines) during detached phase with RMP.

RMP amplitude and location of its resonance layer. **Figure 11(a)** shows the density dependence of the radiated power at different RMP amplitudes quantified by the ratio B_r/B_0 scanned from 0 to 0.12%. The densities at the detachment onset and the radiation collapse are plotted as a function of B_r/B_0 in **Figure 11(b)**. The density range between the detachment transition and thermal collapse corresponds to the operation range with a stable detached plasma. One can see that the density at the collapse is almost independent of the RMP amplitude. With decreasing the amplitude, the detachment transition density shifts to higher density and finally merges with that where the collapse happens. For $B_r/B_0 < 0.07\%$, the RMP is almost completely suppressed by the plasma response, and thus, no stable detachment was realized. As it is seen in **Figure 11(a)**, the radiation level attained in the detached phase is almost independent of the RMP amplitude.

The radial position of the resonance layer of the m/n = 1/1 RMP was scanned by changing the rotational transform ι, which is an inverse value of safety factor q normally used for tokamaks. The radial profiles of T_e for different ι-configurations are plotted in **Figure 12**, where radial shift of the region with a flat T_e profile is demonstrated. As the resonance layer with ι = n/m = 1 moves radially inward, the T_e in the flattening region becomes higher. This is because the island gradually penetrates into the confinement region through the LCFS, and flux surfaces in the island are becoming closed. In the configurations with the magnetic axis at R_{axis} = 3.90 and 3.85 m, the island is marginally outside LCFS and is embedded into the stochastic layer. The stable detachment has been realized so far only for these two configurations. The openness of the flux surfaces in the island thus ensures a low enough level

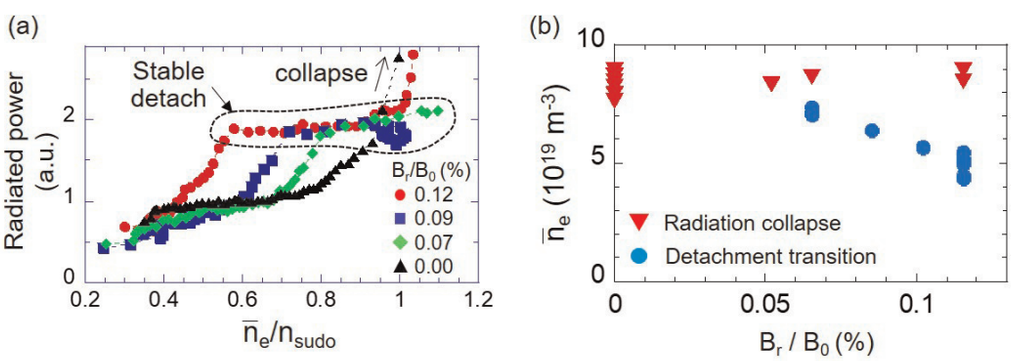


Figure 11.
The radiated power as a function of density for different RMP amplitudes (a) and density at the detachment transition (circles) and radiation collapse (triangles) as a function of RMP amplitude (b).

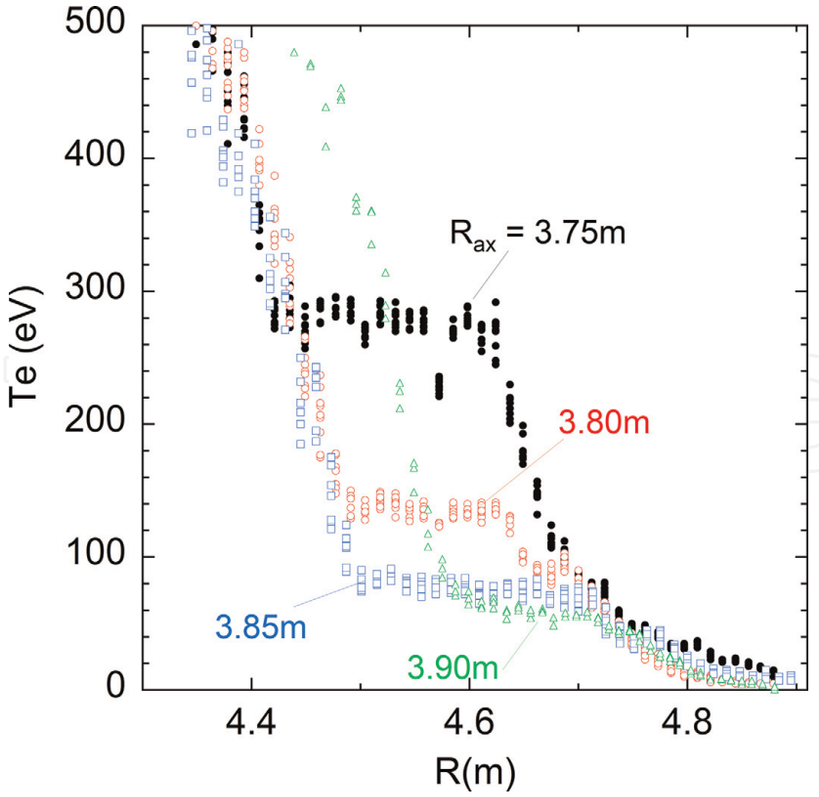


Figure 12.
Radial profiles of T_e for different profiles of the rotational transform. Configurations differ by the position of the magnetic axis, R_{ax}. The stable detachment was realized for R_{ax} = 3.85 and 3.90 m so far.

T_e in the island and consequently a high level of the edge radiation from impurity ions of low charges.

The findings discussed above are summarized in **Figure 13**, where the radial location of the island is represented by the distance between the island X-point and the LCFS [12]. Here, the results from W7-AS are also incorporated. The operation spaces for two devices are not overlapping, which means that probably some hidden parameters important for the detachment stabilization are still missed. Nevertheless, it is seen that for stable sustainment of a detached plasma, there is a threshold value of $\boldsymbol{B_r/B_0}$, which is nearly the same in the LHD and W7-AS, and a certain distance between the island and the confinement region is necessary.

2.5 Compatibility with core plasma performance

The compatibility of a stable detached plasma with a good performance in the plasma core is an important issue for a fusion reactor. Temporal evolution of the radial profiles of T_e, n_e, and the electron pressure measured by Thomson scattering are plotted in **Figure 14**; $\boldsymbol{\overline{n}_e/n_{sudo}}$ = 0.43 and $\geq$ 0.5 correspond to the attached and detached phases, respectively. From the T_e and pressure profiles, one can see the shrinkage of the plasma volume observed as the RMP is applied, which is due to low T_e within the edge magnetic island. It is found that with the RMP application, the increasing density leads to a peaking of the pressure profile. This is due to the increase in n_e at the central region since the T_e profiles are almost the same with and without RMP. The energy confinement time, $\boldsymbol{\tau_E}$, and central pressure, $\boldsymbol{P_{e0}}$, are plotted in **Figure 15**, as functions of the line averaged plasma density [27]. Systematically, $\boldsymbol{\tau_E}$ is smaller with RMP, because of the plasma volume shrinkage. Without RMP, $\boldsymbol{\tau_E}$ becomes saturated around the density limit, while with RMP, it increases with density slightly beyond the density limit. In **Figure 15**, one can see that the pressure peaking with RMP is enhanced especially in the detached phase. Near the

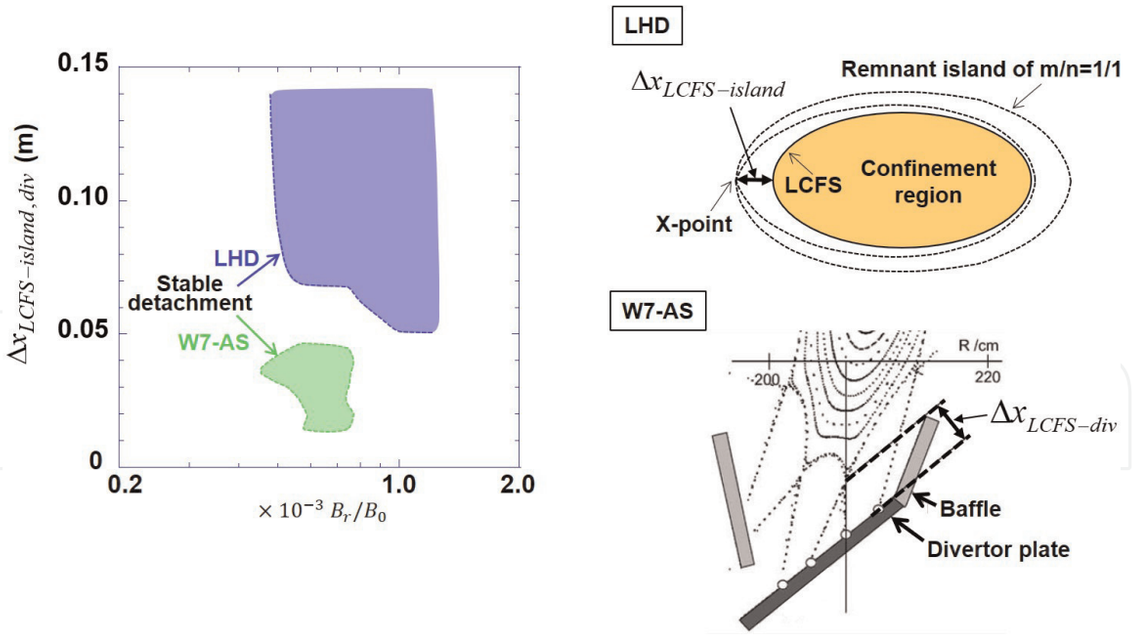


Figure 13.
The operation space in the plane $\Delta x_{LCFS-island}(\Delta x_{LCFS-\mathrm{div}})$, B_r/B_o with a stable detached plasma in the heliotrons LHD and W7-AS [12].

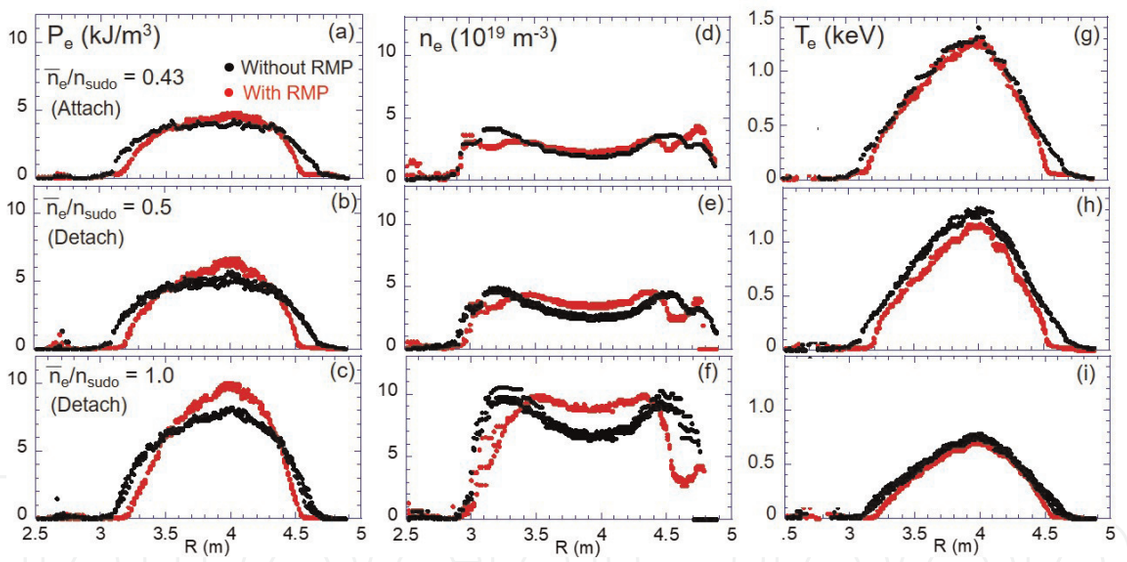


Figure 14.
Radial profiles of (a–c) electron pressure, (d–f) n_e, and (g–i) T_e, with (red) and without (black) RMP, for different densities, $\bar{n}_e/n_{sudo}$ = 0.43, 0.5, and 1.0.

thermal collapse density limit, the fusion triple product, $n_0\tau_E T_0$, becomes comparable for both cases, with and without RMP.

The global parameters are significantly affected by the change in the plasma volume caused by the RMP application. In order to study the local plasma transport characteristics, a core plasma energy transport has been analyzed with the 1-D transport code TASK3D [33]. This code calculates the heating source profile, in the present case by the NBI, by taking into account the beam slowing down and solves a heat conduction equation with $\mathbf{n_e}$ and $\mathbf{T_e}$ values measured experimentally.

Figure 16 shows the resulting NBI power deposition profiles and effective heat conductivity, χ_{eff}=**0**.5(χ_e+χ_i), where χ_e and χ_i are those for electrons and ions and ρ=r_{eff}/a_{99} is the normalized minor radius. In the attached phase, $\bar{n}_e/n_{Sudo}$ = 0.43, the NBI power deposition profiles are almost identical for the both cases with and

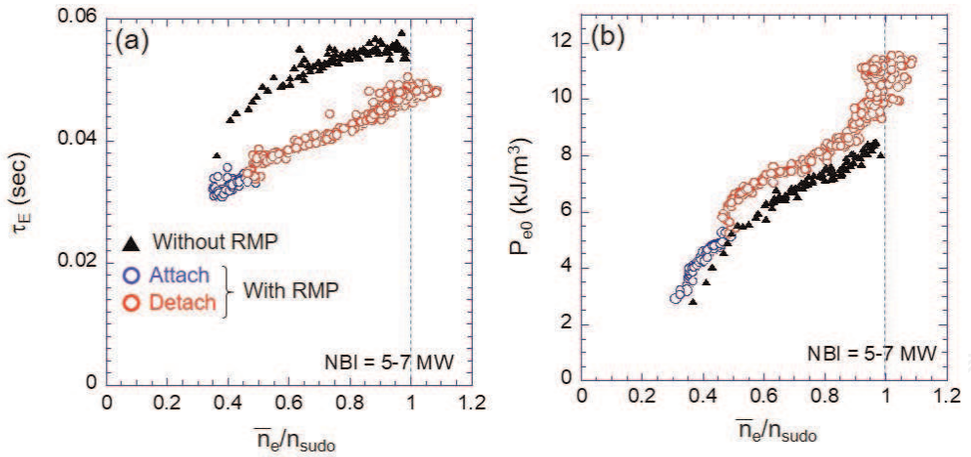


Figure 15.
Density dependence of energy confinement time, τ_E, (a) and of the central pressure, P_{e0}, (b), obtained with (circles) and without (triangles) RMP [27].

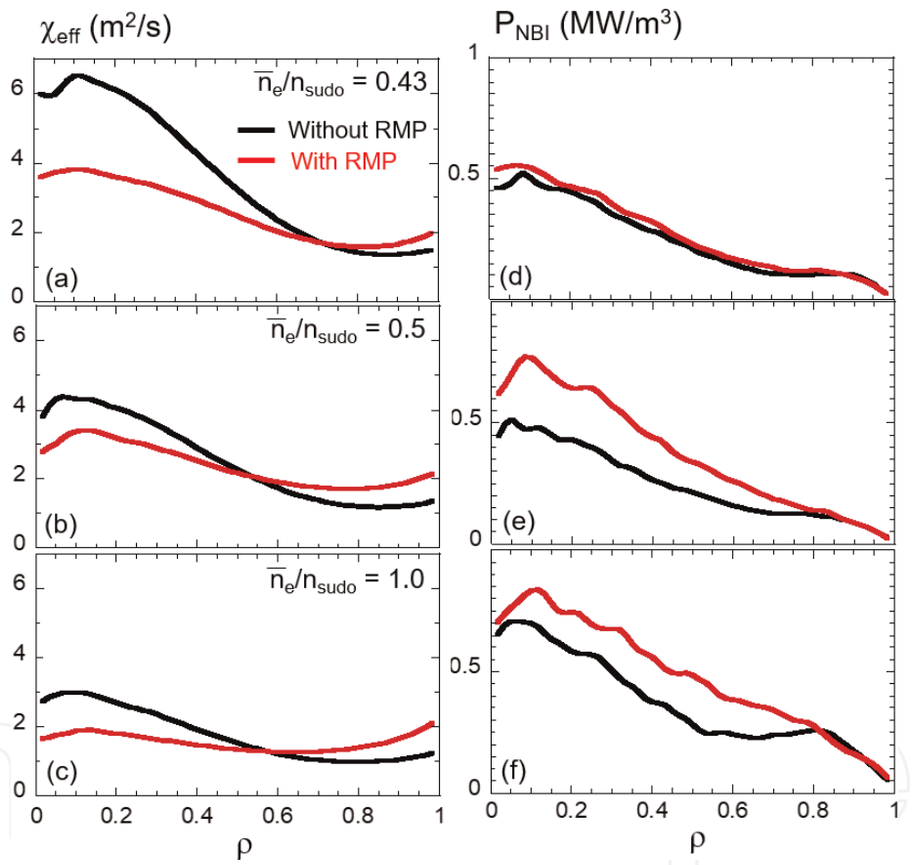


Figure 16.
Radial profiles of (a–c) $\chi_{eff} = 0.5(\chi_e + \chi_i)$, and (d–f) NBI deposition, with (red) and without (black) RMP, for $\overline{n}_e/n_{Sudo}$ = 0.43 (attached), 0.5 (detached), and 1.0 (detached), calculated by core transport code TASK3D.

without RMP, while χ_{eff} is smaller with the RMP in the plasma central region. The larger χ_{eff} in the very core without RMP is attributed to the flat pressure profile there, see **Figure 14(a)**. In the detached phase with $\overline{n}_e/n_{Sudo}$ = 0.50 and 1.0, the NBI heating power is deposited more at the central region with RMP. This is because of a deeper penetration of the NBI due to the shrinkage of the plasma volume with the edge radiation cooling. The increased energy deposition at the central region with RMP, ~0.3 MW/m^3, provides an addition to the particle source density ΔS_p of the order of 10^{19} 1/s/m^3, estimated for an NBI particle energy of 180 keV. According to a simple

picture of a diffusive particle transport, this ΔS_p leads to a density increment of $\Delta n \sim S_p \Delta r^2 / D = 10^{17} \sim 10^{18} m^{-3}$, with $\Delta r \ \ 0.1 \sim 0.4\ m$ $(\Delta \rho \ \ 0.2 \sim 0.8)$, $D = 1\ m^2/s$. This level is too low to be responsible for the density increase of 10^{19} m^{-3} observed at the plasma axis with RMP, **Figure 14(e)** and **(f)**. In the inner plasma region, $\rho < 0.6$, χ_{eff} decreases significantly both with and without RMP with the increasing density, although χ_{eff} remains slightly smaller in the case with RMP. Together with the negligible effects of the NBI particle source, this indicates that the pressure peaking is probably due to the reduction of the transport. On the other hand, at the periphery, $\rho > 0.8$, χ_{eff} becomes larger with RMP. This could be due to additional stochastization caused by the RMP application. Here, the radial transport can be enhanced by flows along braiding magnetic field lines [34, 35]. The larger impurity emission with RMP, see **Figure 7**, could also lead to larger χ_{eff} because TASK3D currently does not take into account the volumetric power loss. The present findings suggest that with the RMP application, there is no significant transport degradation in the central plasma region during the detached plasma phase, compared to the case without RMP.

3. Consideration of detachment as a dissipative structure

The most visible approach to understand the detachment mechanisms is to analyze the power balance at the plasma edge by applying the concept of dissipative structures [36]. The power transported from the plasma core by the plasma heat conduction is lost from the edge region mostly through two channels: (i) the plasma particle outflow through the separatrix and (ii) the radiation of light impurities such as carbon sputtered from the divertor target plates.

On the one hand, the density of the former channel q_{con} is normally monotonously increasing with the plasma temperature T at the plasma edge. On the other hand, it is well known [7] that the impurity radiation density q_{rad} has a maximum as a function of T: by a too low temperature, electrons do not have enough energy to excite impurity species, by a too high temperature, impurities are strongly ionized and have a very large excitation energy. In particular, for carbon, the best "radiators" are the Li-like ions C^{3+}. Qualitatively, q_{con}, q_{rad}, and their sum q_{loss} are displayed as functions of T in **Figure 17**.

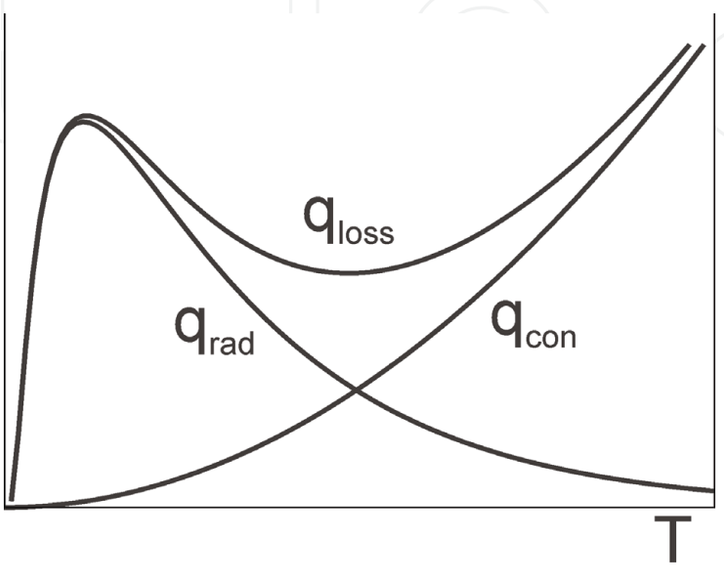


Figure 17.
Temperature dependence for the energy loss channels from the plasma edge with the plasma conduction and convection through the separatrix, q_{con}, with impurity radiation, q_{rad}, and their sum q_{loss}.

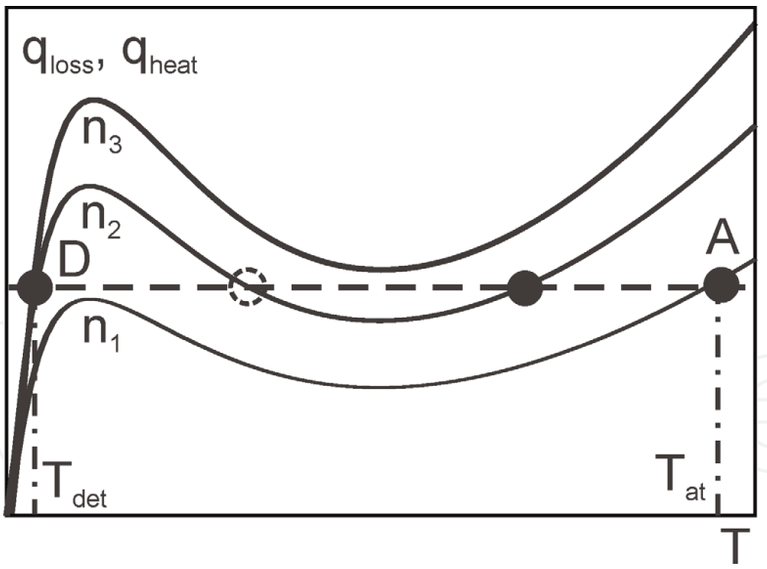


Figure 18.
Temperature dependence for the density of the energy loss from the plasma edge, q_{loss}, for three magnitudes of the plasma density $n_1 < n_2 < n_3$ (solid curves) and of the heat flux to the edge from the plasma core, q_{heat}. In a steady state, these balance each other, $q_{loss} = q_{heat}$.

Both q_{con} and q_{rad} increase with plasma density n [7]. Indeed, the larger the content of plasma particles, the higher their loss from the device. Likewise, q_{rad} increases both with the density of exciting electrons n and that of the exciting impurity species $n_I = c_I n$. Typically, the relative concentration c_I of carbon impurityin LHD plasmas is of order of 1%.

In a steady state, the energy loss from the plasma edge has to be balanced by the heat transfer from the plasma core, with the density q_{heat}, which in many cases is weakly dependent both on the edge temperature and on the plasma density. **Figure 18** shows q_{loss} and q_{heat} versus T for three magnitudes of n. One can see that a moderate increase of the plasma density from n_1 to n_3, by less than 40%, results in a very strong drop in the stationary edge temperature, from its level T_{at} of several tens of eVs in an attached plasma state A to T_{det} of $1\,eV$ in a detached state D. In the latter case, electrons and ions in the plasma effectively recombine one with another as it is indicated by spectroscopic measurements.

For the intermediary level of the density, n_2, there are three steady states. It is straightforward to comprehend that the one with the in-between temperature is unstable. Indeed, an infinitesimal spontaneous deviation from this state, e.g., with diminishing T, leads to an increase of the energy losses and a further decrease of the edge temperature. Finally, the plasma will get the one of two stable states with a low temperature.

4. Nonlinear low-frequency oscillations at the detachment onset

As it was discussed in the first part of the present chapter, there is a significant difference between the detachment scenario in LHD without and with RMP. In the former case, one needs very fine tuning of the radiation level by gas puffing of fuel or impurity, and detachment onset may lead to a total radiation collapse of the discharge. Unlikely, with RMP after the transition to the detached state, the plasma density can be increased further, with corresponding growth of the radiated power and without a significant deterioration of the discharge performance. Finally, a radiation collapse occurs roughly at the same plasma density as without RMP.

Interestingly, that by the detachment onset with RMP, there is some density range where nonlinear oscillations of high amplitude and relatively low frequency of 100 Hz have been observed in diverse plasma parameters such as the radiation intensity and ion saturation current to the divertor target plates. Also in tokamaks, similar large-scale self-sustained periodic oscillations in various plasma characteristics have been seen, by approaching to critical conditions, see, for example, [37, 32]. Several models [38–40] have been proposed previously to explain these phenomena.

Here, we consider two new mechanisms. The first one is relevant for LHD, with plasma of relatively low density in its divertor legs. In such a situation, by approaching to the critical density, the plasma detaches practically directly from the periphery of the edge stochastic layer. This reminds the phenomenon of radial detachment in limiter tokamaks such as TFTR and TEXTOR. The threshold conditions for radial detachment have been analyzed in [41].

The second mechanism is pertinent for the case of tokamaks with divertors like JET, ASDEX-U, DII-D, operating before detachment in the regime of strong plasma recycling on the target plates [7].

4.1 Radial detachment

4.1.1 Stationary states

In the simplest case, the behavior of the plasma temperature T in the edge region is governed by the following heat conduction equation:

$$3n\partial_t T + \partial_x q_x = -c_I n^2 L_{rad} \tag{1}$$

where $q_x = -\kappa_\perp \partial_x T$ is the density of heat flux perpendicular to the magnetic surfaces, in the direction x, with $\kappa_\perp$ being the corresponding component of the plasma heat conduction; the term on the right-hand side (rhs) is the energy loss due to impurity radiation, whose temperature dependence is determined by that of the cooling rate L_{rad}. The behavior described qualitatively in the previous section is well mimicked by the following formula [41]:

$$L_{rad} = L_{rad}^{\max} \exp\left[-\left(\sqrt{T_1/T} - \sqrt{T/T_2}\right)^2\right] \tag{2}$$

For carbon impurity, dominating the radiation losses from the plasma edge in LHD, $L_{rad}^{\max} \approx 6.6 \times 10^{-7} eV\ cm^3 s^{-1}$, $T_1 \approx 5eV$, $T_2 \approx 64eV$. In Eq. (1), we assume n, $\kappa_\perp$, and c_I invariable in time and space.

Subsequently, we multiply Eq. (1) with $2\kappa_\perp \partial_x T$ and integrate over the coordinate x, from the interface with plasma core, $x = x_c$, to the outer boundary of the stochastic layer, $x = x_s$. As a result, one gets

$$6n \int_{x_c}^{x_s} q_x \partial_t T dx = P(T_s) \equiv q_c^2 - q_s^2 - 2\kappa_\perp c_I n^2 \int_{T_s}^{T_c} L_{rad}(T) dT \tag{3}$$

where $T_{c,s} = T(x_{c,s})$, $q_c = q_x(x_c)$ is given by the heating power transported from the core to the edge region; $q_c = q_x(x_c) = \kappa_\perp T_s/\delta_s$ is prescribed as a boundary condition [41, 42], with the temperature e-folding length δ_s at the separatrix defined by the transport in the SOL with open field lines and being fixed in the present analysis. By assessing the term on the left-hand side (lhs), we adopt for q_x its value average in the

edge region, $(q_c + q_s)/2$. Furthermore, it is reasonable to assume that by the oscillations in question the strongest time variation in the temperature occurs close to the outer boundary and $\partial_t T_s$ makes the largest contribution to the integral on the lhs of Eq. (3). In average over the edge we assume $\partial_t T \approx \frac{\partial_t T_s}{2}$ and the lhs of Eq. (3) is estimated as $C\partial_t T_s$, with $C(T_s) \approx 1.5n(x_s - x_c)(q_c + q_s)$. Normally $T_c = T(x_c) \approx 300 - 400\ eV \gg T_2$ and the integral in the rhs is practically unaffected by the upper integration limit. Finally, from Eq. (3) one gets the following equation for $T_s(t)$:

$$dT_s/dt \approx P(T_s)/C(T_s) \tag{4}$$

In **Figure 19**, the rhs of Eq. (4) is displayed for $q_c = 80\ kW\ m^{-2}$, $\kappa_\perp = 8 \times 10^{19}\ m^{-1}\ s^{-1}$, $\delta_s = 0.02\ m$, $x_s - x_c = 0.2\ m$, $c_I = 0.01$, $n = 8 \times 10^{19}\ m^{-3}$ and $n = 10^{20}\ m^{-3}$, parameters typical for the conditions of experiments aimed on the investigation of the detachment process in LHD [20].

4.1.2 Time evolution at the plasma density above the critical one

According to **Figure 19,** if a critical plasma density of $9 \times 10^{19}\mathrm{m}^{-3}$ is exceeded, no stationary state can be sustained for the assumed impurity concentration $c_I = 0.01$. The latter, however, does not remain at the same level since the plasma detachment from divertor target plates leads to the vanishing of the impurity source due to physical and chemical sputtering of the plate material [7]. As a result, impurities diffuse out of the plasma core and their concentration decreases. The characteristic time for the impurity concentration decay is of $\tau_I \approx l_I^2/D_\perp$, where l_I is the characteristic penetration depth of the mostly radiating Li-like ions of carbon and $D_\perp$ is the charged particle diffusivity. Impurity transport analysis [42] shows that if $l_I \approx 0.05 - 0.1$ m and for $D_\perp \approx 0.5\ \mathrm{m}^2\ \mathrm{s}^{-1}$, we get $\tau_I \approx 5 - 20$ ms. In the simplest way, the time evolution of impurity concentration can be described by the equation:

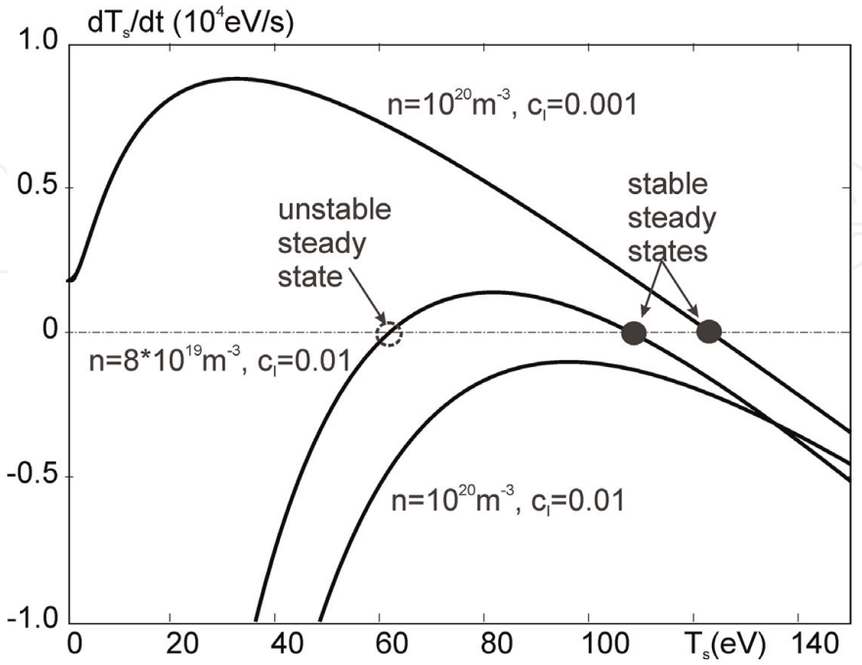


Figure 19.
Dependence of time derivative of the plasma temperature at the outer boundary of the stochastic layer, x_s, the rhs of Eq. (3), on T_s for different plasma density and impurity concentration. Steady states, $dT_s/dt = 0$ with $\frac{\partial}{\partial T_s}\frac{dT_s}{dt} > 0$, $\frac{\partial}{\partial T_s}\frac{dT_s}{dt} < 0$ (black circles) are stable and that with $d^2T_s/dt^2 < 0$ (transparent circle) are unstable.

$$dc_I/dt = \left[c_I^0(T_s) - c_I\right]/\tau_I \tag{5}$$

For the stationary impurity concentration, we assume $c_I^0\left(T_s \geq T_s^*\right) = 10^{-2}$ and $c_I^0\left(T_s < T_s^*\right) = 10^{-3}$ with $T_s^* \approx 5$ eV. **Figure 20** demonstrates the time evolution of the impurity concentration c_I and of the radiation level q_{rad}/q_c, calculated for $n = 10^{20}$ m^{-3} and $\tau_I = 15$ ms. Without knowing the exact temperature profile $T(x)$, needed to assess the flux density of radiation losses q_{rad} firmly, we estimated this by assuming a linear one $T(x) = [T_s(x - x_c) + T_c(x_s - x)]/(x_s - x_c)$.

One can see that the frequency of these oscillations is of 100 Hz, in agreement with observations.

By concluding this section, we discuss qualitatively possible causes for the difference in the behavior of the detached plasma in LHD without and with RMP, respectively, an unstoppable penetration of cold plasma into the core, leading to the radiation collapse, and the existence of the plasma density range where the radiation layer is stably confined at the plasma edge. As it has been demonstrated in [42], the mechanisms both of plasma heating and heat transfer through the plasma are of the importance for the discharge behavior by achieving the critical density. In ohmically heated discharges in the tokamak TEXTOR, where the plasma current was maintained at a preprogrammed level, a radial detachment was stopped by the increase in the density of the heat flux from the hot plasma core due to decreasing minor radius of the current carrying plasma column. If, however, the main heating is predominantly supplied from other sources such as NBI, this stabilization mechanism is ineffective and, as calculations in [42] have shown, a radiation collapse occurs, similar as this happens in LHD without RMP.

What occurs as a detachment set is determined by the competition between the decay of the impurity concentration in the plasma, characterized by the time τ_I, and time for the cooling front spreading into the plasma core. As it has been discussed in the first part, in addition to the magnetic island with strongly increased transport, RMP induce a region deeper into the plasma core. With the experimentally measured T_e profiles, one can assess that with the RMP, the heat conduction in this region is reduced by a factor of 10 and the heat conductivity $\chi_\perp = \kappa_\perp/n$ is of 1 m^2 s^{-1}. For the penetration of the cooling front through this region, with a width Δ of 0.15 m, a time of $\Delta^2/\chi_\perp \approx 20$ ms is needed. This is at the upper limit of the impurity decay time, and

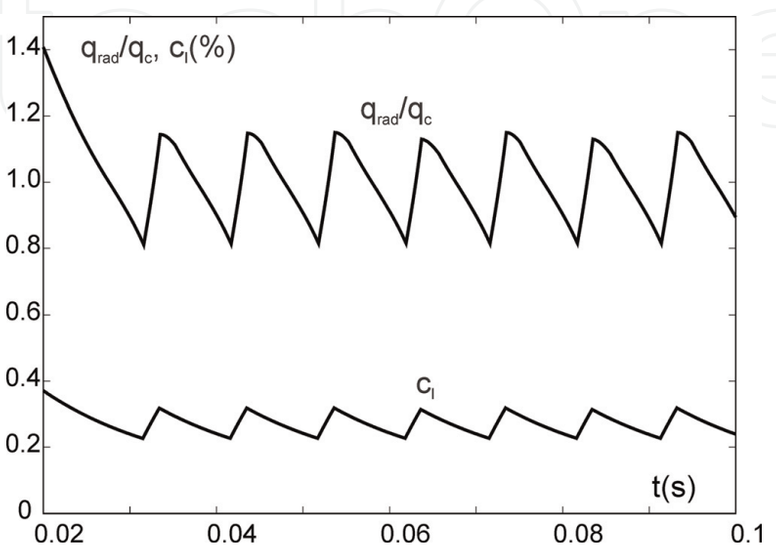


Figure 20.
The time evolution of the impurity radiation level q_{rad}/q_c and concentration, calculated by integrating Eqs. (4) and (5) for $n = 10^{20}$ m^{-3} and $\tau_I = 15$ ms.

therefore, the cooling wave most probably fades out. This mechanism is to some extend similar to that of the excitation of self-sustained oscillations in a plasma-wall system with strongly inhomogeneous diffusivity of charged particles [40].

4.2 Model for self-sustained oscillations by detachment in the regime of strong recycling on divertor targets

4.2.1 Stationary states in the recycling zone near the target

In a stationary state, the plasma parameters, such as electron density n and temperature T, near the divertor target are governed by the particle and heat balances in the recycling zone (RZ), see **Figure 21**. On the one hand, the heat flux transported to the RZ by plasma heat conduction and convection is dissipated by the energy loss (i) with the plasma outflow to the target, (ii) by the ionization and excitation of recycling neutrals, and transfer of the thermal energy of neutrals, escaping from the plasma layer, $|x| \le \delta_p/2$, to gas particles:

$$q_r \delta_p = \gamma T_t \Gamma_t \delta_p + E_{ion}\left(\Gamma_t \delta_p - J_a\right) + 1.5 J_a T_r \tag{6}$$

Here, q_r is the heat influx into RZ projected onto the normal to the target, γ is the heat transmission factor, $\Gamma_t = n_t c_s \sin\psi$ is the same projection for the plasma particle outflow to the target, $c_s = \sqrt{2T_t/m_i}$ is the ion sound velocity, n_t, T_t are the plasma density and temperature near the target, ψ is the inclination angle of the magnetic field to the target, E_{ion} is the energy spent on the ionization of an atom, and J_a is the density of the atom outflow from the plasma layer.

In addition to Eq. (6), the particle balance in the RZ has to be fulfilled in a stationary state:

$$\Gamma_r \delta_p = J_a \tag{7}$$

where Γ_r is normal to the target projection of the influx into the RZ of charged particles from the main SOL. To assess J_a, one has to consider behavior of atoms, recycling from the target. In the plasma layer, $|x| \le \delta_p/2$, these are ionized by

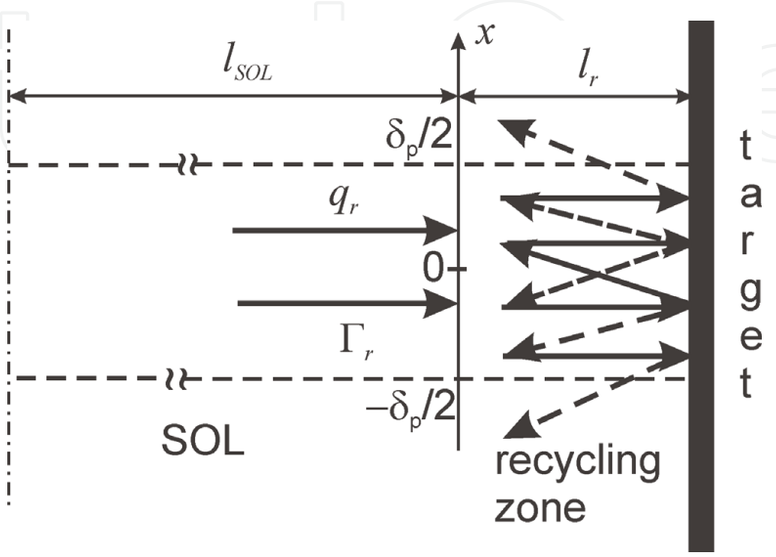


Figure 21.
A schematic view of the charged and neutral particle flows in the recycling zone (RZ) in vicinity of a divertor target plate; q_r and Γ_r are the projections normal to the target of the densities of heat and charged particle influxes into the RZ from the main SOL.

electrons and charge-exchange (cx) with ions. The cx rate coefficient k_{cx} is noticeably larger than that for ionization, k_{ion}. Thus, during the lifetime, recycling atoms many times chaotically changes the velocity direction; i.e., their motion near the target is like Brownian one. Quantitatively, it is described by the diffusivity:

$$D_a = V_i \lambda_a = V_i^2 / [(k_{cx} + k_{ion}) n_r] \tag{8}$$

where $V_i = \sqrt{T_r, /m_i}$ is the ion thermal velocity, which atoms acquire after a cx collision, λ_a is the mean free path length of atoms, and n_r, T_r are the characteristic plasma density and temperature in the RZ, which we have to define.

The width l_r of the recycling zone, **Figure 21**, is defined roughly as a distance from the target where the atom density $n_a(x,l)$ decays to a low enough level, e.g., by a factor of 10. By integrating over $0 \le l \le l_r$, the continuity equation is reduced to the following one for the variable $N_a(x) = \int_0^{l_r} n_a(x,l)dl$:

$$-D_a d^2 N_a / dx^2 = \Gamma_t - k_{ion} n_r N_a \tag{9}$$

The boundary conditions presume that atoms escape out of the plasma layer with their thermal velocity. With constant D_a and k_{ion}, corresponding to n_r, T_r, one finds an analytical solution to the equation above and gets:

$$J_a = \left[N_a\left(\frac{\delta_p}{2}\right) + N_a\left(-\frac{\delta_p}{2}\right) \right] \mathrm{V}_i = \frac{\delta_p \Gamma_t}{\chi_{ion} + \chi_{dif} / \tanh \chi_{dif}} \tag{10}$$

with $\chi_{ion} = \delta_p k_{ion} n_r / (2V_i)$, $\chi_{dif} = \chi_{ion} \sqrt{1 + k_{cx}/k_{ion}}$.

For fixed q_r and Γ_r, Eqs. (6), (7), and relation (10) allow to determine the plasma parameters in the RZ, by taking into account that $n_r \approx n_t$, $T_r \approx T_t$. For $q_r = 5\mathrm{kW/cm^2}$, $\delta_p = 5$ cm and $\psi = \pi/2$, **Figure 22** shows n_r, T_r calculated as functions of Γ_r.

4.2.2 The plasma particle influx into RZ and stability analysis of stationary states

The density of the charged particle influx into the RZ, Γ_r, is defined by the transfer of plasma particles and momentum along the magnetic field in the main part of the SOL. In a zero-dimensional approximation, these are as follows:

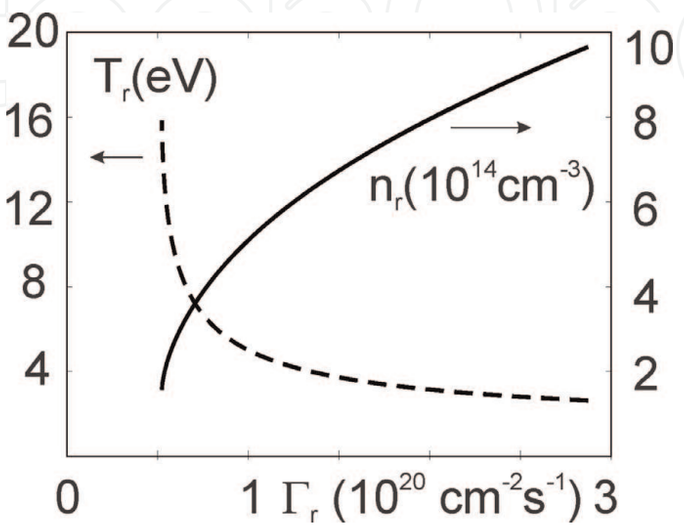


Figure 22.
The Γ_r dependence of the plasma parameters in the recycling zone calculated for $= \pi/2$, $q_r = 5kW/cm^2$, and $\delta_p = 5$ cm.

$$\frac{dn_{SOL}}{dt} = S_\perp - \frac{\Gamma_r}{l_{SOL}}, \frac{d\Gamma_r}{dt} = \frac{2n_{SOL}T_{SOL} - M_r}{m_i l_{SOL}} \tag{11}$$

where n_{SOL} and T_{SOL} are the characteristic plasma density in the main SOL, far from the target, and $S_\perp$ is the plasma source density due to losses from the confined plasma through the separatrix. The SOL extension in the poloidal direction, l_{SOL}, is much longer than that of RZ, l_r, and therefore, a characteristic time for Γ_r change is much larger than that for n_r, T_r. Thus, the latter are always governed by quasi-stationary Eqs. (6) and (7). The total momentum at the entrance of the RZ is,

$$M_r = 2n_r T_r + \frac{m_i}{n_r}\left(\frac{\Gamma_r}{\sin\psi}\right)^2 \tag{12}$$

In a stationary state, $dn_{SOL}/dt = d\Gamma_r/dt = 0$ and $\Gamma_r^{st} = S_\perp l_{SOL}$, $n_{SOL}^{st} = M_r\left(\Gamma_r^{st}\right)/(2T_{SOL})$.

To analyze the stability of stationary states, we assume as usually that there is a spontaneous small deviation from such a state, i.e., $\Gamma_r(t) = \Gamma_r^{st} + \delta\Gamma_r \exp(\gamma t)$ and $n_{SOL}(t) = n_{SOL}^{st} + \delta n_{SOL} \exp(\gamma t)$. Due to strong dependence of the parallel heat conduction on the temperature, $\kappa_\parallel \sim T^{2.5}$, T_{SOL} is considered as unperturbed. By substituting these forms of $\Gamma_r(t)$, $n_{SOL}(t)$ into Eq. (11) and requiring that the resulting system of linear equations for $\delta\Gamma_r$ and δn_{SOL} has a nontrivial solution, one gets a quadratic algebraic equation for the growth rate γ with the solutions:

$$\gamma = -\omega_r/2 \pm \sqrt{\omega_r^2/4 - \omega_s^2} \tag{13}$$

where $\omega_r = \frac{\partial M_r/\partial\Gamma_r}{m_i l_{SOL}}$ and $\omega_s = \frac{\sqrt{2T_{SOL}/m_i}}{l_{SOL}}$. Usually, $|\omega_r| \ll \omega_s$, i.e., the second term in γ is imaginary and defines the frequency for small oscillations. Thus, Reγ>0 for $\omega_r \sim \partial M_r/\partial\Gamma_r < 0$, and the corresponding states with the negative slope of the $M_r(\Gamma_r)$ dependence are unstable. **Figure 23** shows this dependence for the parameter magnitudes used to calculate the results presented in **Figure 22**. In addition, we display by the dashed curve the $M_r(\Gamma_r)$ dependence obtained, by taking into account the energy losses on ionization and excitation of carbon impurity eroded from the target plate by physical and chemical sputtering, see [7]. The vertical lines correspond to Γ_r^{st} for different $S_\perp$. For the larger one, the stationary state is unstable.

It is of interest to consider how $M_r(\Gamma_r)$ dependence changes with the magnitude of q_r and **Figure 24** demonstrates this. For low enough q_r, the losses on ionization of all recycling neutrals, the second term on the right-hand side of Eq. (6), exceed significantly the heat influx into the RZ, and atoms freely escape into the gas, i.e., $\Gamma_r \approx n_t c_s \sin\psi$ and $M_r \approx 4n_t T_t \approx \frac{4\sqrt{q_r\Gamma_r m_i}}{\sqrt{2\gamma+3}\sin\psi}$.

For large enough q_r, practically all recycling atoms are ionized in the plasma layer and Eq. (6) provides $n_r \approx q_r/[c_s \sin\psi(E_{ion} + \gamma T_r)]$ and $M_r \approx 2n_r T_r \approx \frac{q_r\sqrt{2T_r m_i}}{\sin\psi(E_{ion}+\gamma T_r)}$.

Thus, as a function of T_r, M_r has a maximum at $T_r = E_{ion}/\gamma$. Because of the unique relation between Γ_r and T_r, a maximum exists also for the $M_r(\Gamma_r)$ dependence. For a stationary state with $\partial M_r/\partial\Gamma_r < 0$, the instability would lead to an enduring increase of Γ_r and n_r and decrease of T_r. A new steady state can be achieved due to mechanisms, which are not taken into account in the present model, e.g., recombination of charged particles. In [38], the maximum in $M_r(T_r)$ has been interpreted as a density limit in the main SOL. Indeed, since in the case of interest $M_r \approx 2n_{SOL}T_{SOL}$ and T_{SOL} is changing very weakly, n_{SOL} cannot exceed $M_r^{\max}/(2T_{SOL})$.

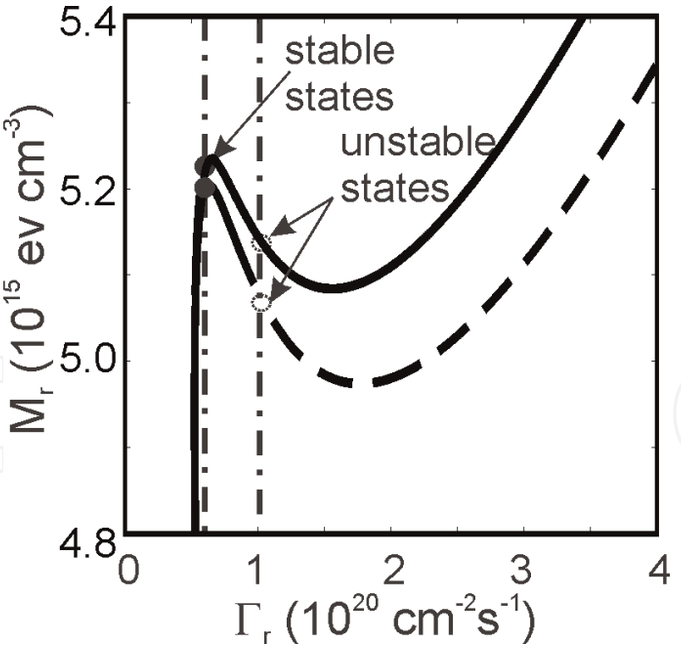


Figure 23.
M_r versus Γ_r calculated for $q_r = 5kW/cm^2$, $\delta_p = 5$ cm and $\psi = \pi/2$, without (solid curve) and with (dashed curve) impact of C impurity eroded from the target. Vertical lines correspond with stationary Γ_r^{st} values for different $S_\perp$. The states with larger Γ_r^{st} are unstable.

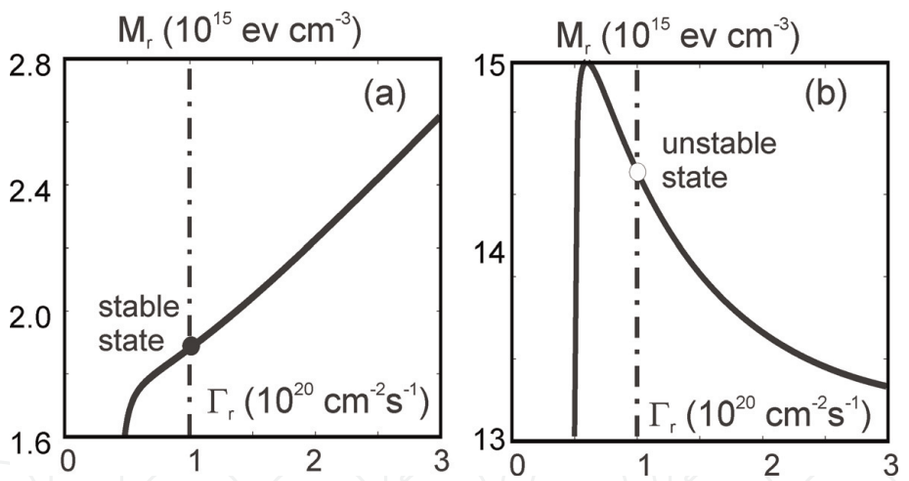


Figure 24.
$M_r(\Gamma_r)$ computed for $q_r = 1.5kW/cm^2$ (a) and $15kW/cm^2$ (b). For the same, $\Gamma_r^{st} = 10^{22}\ cm^{-2}\ s^{-1}$ stationary states can be both stable (a) and unstable (b).

4.2.3 Limit cycle nonlinear oscillations

The case of the intermediate $q_r = 5\text{kW/cm}^2$ presented in **Figure 23** is considered qualitatively. The plasma in the RZ, being initially in the unstable stationary state with $\Gamma_r^{st} = 10^{20}$ cm^{-2} s^{-1}, will deviate from this along the $M_r(\Gamma_r)$ curve to one of its optima, e.g., to the maximum point A, **Figure 25**. Here, Γ_r is smaller than its stationary level and $dn_{SOL}/dt>0$, see Eq. (11). The increase in n_{SOL} leads to $d\Gamma_r/dt>0$, and Γ_r also increases till the trajectory in the (Γ_r, M_r) phase plane comes to the point B at the stable branch on the $M_r(\Gamma_r)$ curve. Here, both dn_{SOL}/dt and $d\Gamma_r/dt$ are negative and Γ_r, M_r decrease to the minimum point C. Since in this point $d\Gamma_r/dt$ is still negative, a development till the point D on the left stable branch of the $M_r(\Gamma_r)$ curve takes place. Here, $d\Gamma_r/dt>0$ and Γ_r, M_r increase till the point A.

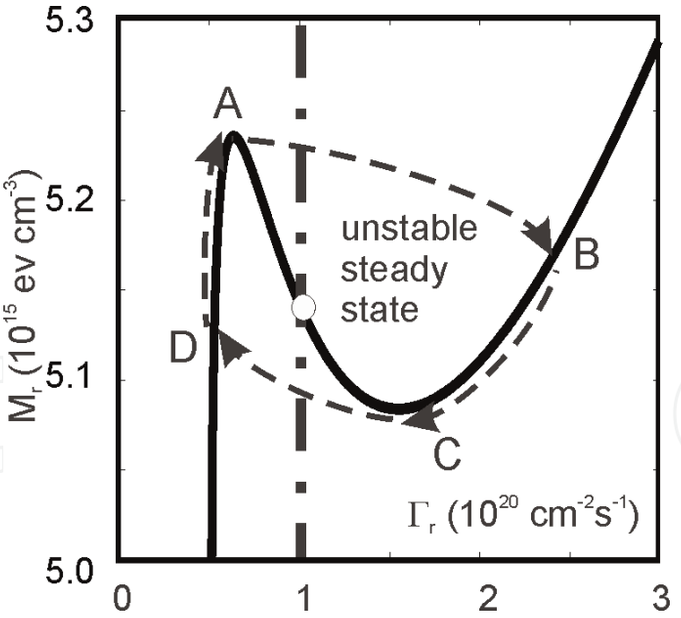


Figure 25.
Schematic view of the limit cycle oscillations around an unstable steady state at $q_r = 1.5kW/cm^2$ and $\Gamma_r^{st} = 10^{22}\ cm^{-2}\ s^{-1}$.

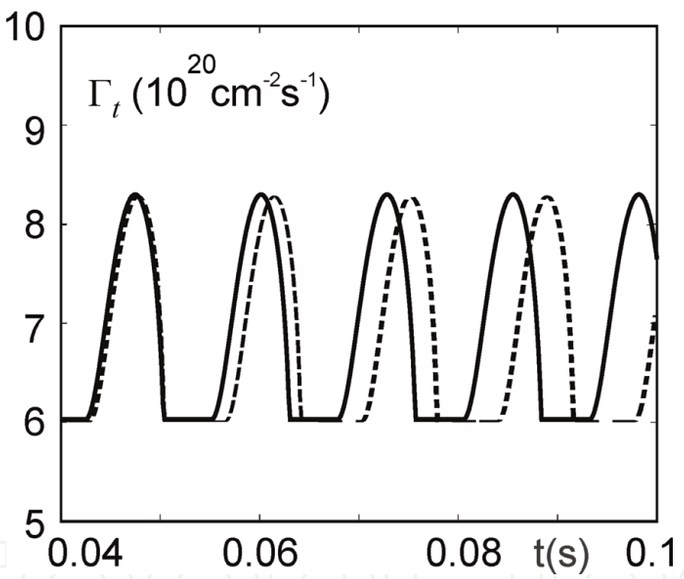


Figure 26.
Time evolution of the plasma flux density onto the target, Γ_t, obtained by numerical integration of Eq. (11) for the unstable steady state at $q_r = 1.5kW/cm^2$ and $\Gamma_r^{st} = 10^{22}\ cm^{-2}\ s^{-1}$ without (solid curve) and with (dashed curve) impact of C impurity eroded from the target.

Thus, nonlinear oscillations around the unstable stationary point arise. In **Figure 26**, the time evolution for the flux density onto the target, $\Gamma_t(t)$, for the set of input parameters as for **Figure 25** is presented.

5. Conclusions

Plasma detachment from divertor targets is an important and very interesting phenomenon in fusion devices including helical systems and tokamaks. On the one hand, it can lead to the deterioration of the plasma performance and even to the total collapse of the discharge. On the other hand, detachment, if it is controlled and

stable can be useful for the reduction of the heat power losses to the target plates and even may lead to peaking of the pressure profiles in the plasma core that manifests in a confinement improvement. Resonant magnetic perturbations providing a broad enough magnetic island close to the separatrix has proven to be an effective method to control detachment in LHD.

Often at the onset of the detachment, large nonlinear oscillations of relatively low frequency can be observed in different plasma parameters, such as radiated power and ion saturation current to the target plates. Two models of such self-sustained oscillations are proposed. The first one is relevant to the radial detachment in LHD with divertor legs of low plasma density and transparent for neutrals. The second model offers an explanation for phenomena in tokamaks observed at the transition from strong recycling to plasma detachment at divertor targets.

Acknowledgements

The authors are grateful for the fruitful discussions with Prof. S. Masuzaki, Prof. S. Morita, Dr Y. Narushima, Prof. N. Ohno, Prof. B.J. Peterson, Prof. R. Sakamoto, Dr R. Seki, Dr H. Tanaka, Dr T. Tokuzawa, Prof. K.Y. Watanabe, Prof. H. Yamada, Dr I. Yamada, Prof. M. Yokoyama, Dr. J.W. Ahn, Dr Y. Feng, Prof. K. Ida, Prof. K. Itoh, Prof. S. Kajita, Dr G. Kawamura, Prof. T. Morisaki, Dr K. Mukai, Dr K. Nagaoka, Prof. M. Osakabe, Dr H. Takahashi, and Prof. K. Tanaka. The authors also thank the LHD experimental group for the excellent operation of LHD. The work has been financially supported by JSPS KAKENHI with grant numbers JP16H04622 and JP19H01878 and NIFS budget code ULPP026.

Author details

Masahiro Kobayashi[1,2*] and Mikhail Tokar[1,3]

1 National Institute for Fusion Science, National Institutes of Natural Sciences, Toki, Japan

2 Department of Fusion Science, SOKENDAI, Toki, Japan

3 Institute for Energy and Climate Research—Plasma Physics, Jülich Research Centre, Germany

*Address all correspondence to: kobayashi.masahiro@nifs.ac.jp

IntechOpen

© 2019 The Author(s). Licensee IntechOpen. This chapter is distributed under the terms of the Creative Commons Attribution License (http://creativecommons.org/licenses/by/3.0), which permits unrestricted use, distribution, and reproduction in any medium, provided the original work is properly cited. CC BY

References

[1] Pitts RA et al. Physics basis for the ITER tungsten divertor. Nuclear Materials and Energy

[2] Asakura N et al. Studies of power exhaust and divertor design for a 1.5 GW-level fusion power DEMO. Nuclear Fusion. 2017;**57**:126050. DOI: 10.1088/1741-4326/aa867a

[3] Takeiri Y et al. Realization of high T i plasmas and confinement characteristics of ITB plasmas in the LHD deuterium experiments. Nuclear Fusion. 2018;**58**: 106028. DOI: 10.1088/1741-4326/aad87e

[4] Wolf RC et al. Major results from the first plasma campaign of the Wendelstein 7-X stellarator. Nuclear Fusion. 2017;**57**:102020. DOI: 10.1088/1741-4326/aa770d

[5] Evans TE et al. 3D vacuum magnetic field modelling of the ITER ELM control coil during standard operating scenarios. Nuclear Fusion. 2013;**53**: 093029. DOI: 10.1088/0029-5515/53/9/093029

[6] Schmitz O et al. Three-dimensional modeling of plasma edge transport and divertor fluxes during application of resonant magnetic perturbations on ITER. Nuclear Fusion. 2016;**56**:066008. DOI: 10.1088/0029-5515/56/6/06600

[7] Stangeby PC. The Plasma Boundary of Magnetic Fusion Devices. Bristol, Philadelphia: Institute of Physics Publishing; 2000

[8] Shimomura Y et al. Characteristics of the divertor plasma in neutral-beam-heated ASDEX discharges. Nuclear Fusion. 1983;**23**:869. DOI: 10.1088/0029-5515/23/7/002

[9] Masuzaki S et al. The divertor plasma characteristics in the large helical device. Nuclear Fusion. 2002;**42**:750. DOI: 10.1088/0029-5515/42/6/313

[10] Feng Y et al. Physics of island divertors as highlighted by the example of W7-AS. Nuclear Fusion. 2006;**46**: 807. DOI: 10.1088/0029-5515/46/8/006

[11] Kobayashi M et al. Transport characteristics in the stochastic magnetic boundary of LHD: Magnetic field topology and its impact on divertor physics and impurity transport. Fusion Science and Technology. 2010;**58**:220. DOI: 10.13182/FST10-A10809

[12] Kobayashi M et al. 3D effects of edge magnetic field configuration on divertor/scrape-off layer transport and optimization possibilities for a future reactor. Nuclear Fusion. 2015;**55**:104021. DOI: 10.1088/0029-5515/55/10/104021

[13] Ezumi N et al. Experimental observation of plasma flow alternation in the LHD stochastic magnetic boundary. Journal of Plasma and Fusion Research Series. 2009;**8**:429

[14] Feng Y et al. Comparative divertor-transport study for helical devices. Nuclear Fusion. 2009;**49**:095002. DOI: 10.1088/0029-5515/49/9/095002

[15] Kobayashi T et al. Three dimensional distribution of impurity emission in the edge region of LHD obtained by single field-of-view tomography. Nuclear Materials and Energy. 2019;**19**:239. DOI: 10.1016/j.nme.2019.02.015

[16] Zhang HM et al. Estimation of partial carbon radiation at each ionization stage of C2+ to C5+ ions in large helical device. Plasma and Fusion Research. 2016;**11**:2402019

[17] Tanaka H et al. Toroidally symmetric/asymmetric effect on the divertor flux due to neon/nitrogen seeding in LHD. Nuclear Materials and Energy. 2017;**12**:241. DOI: 10.1016/j.nme.2016.12.020

[18] Mukai K et al. Development of impurity seeding and radiation enhancement in the helical divertor of LHD. Nuclear Fusion. 2015;**55**: 083016. DOI: 10.1088/0029-5515/55/8/083016

[19] Kawamura G et al. Three-dimensional impurity transport modeling of neon-seeded and nitrogen-seeded LHD plasmas. Plasma Physics and Controlled Fusion. 2018;**60**:084005. DOI: 10.1088/1361-6587/aac9ea

[20] Kobayashi M et al. Control of 3D edge radiation structure with resonant magnetic perturbation fields applied to the stochastic layer and stabilization of radiative divertor plasma in LHD. Nuclear Fusion. 2013;**53**:093032. DOI: 10.1088/0029-5515/53/9/093032

[21] Pandya SN et al. Dynamics of three-dimensional radiative structures during RMP assisted detached plasmas on the large helical device and its comparison with EMC3-EIRENE modeling. Nuclear Fusion. 2016;**56**:046002. DOI: 10.1088/0029-5515/56/4/046002

[22] Zhang HM et al. Vertical profiles and two-dimensional distributions of carbon line emissions from $C2^{+}-C5^{+}$ ions in attached and RMP-assisted detached plasmas of large helical device. Physics of Plasmas. 2017;**24**:022510. DOI: 10.1063/1.4976989

[23] Ohyabu N et al. The large helical device (LHD) helical divertor. Nuclear Fusion. 1994;**34**:387. DOI: 10.1088/0029-5515/34/3/i07

[24] Kobayashi M et al. Core plasma confinement during detachment transition with RMP application in LHD. Nuclear Materials and Energy. 2018;**17**: 137. DOI: 10.1016/j.nme.2018.10.003

[25] Narushima Y et al. Magnetic diagnostics of magnetic island in LHD. Plasma and Fusion Research. 2007;**2**: S1094

[26] Narushima Y et al. Behavior of plasma response field in detached plasma. Plasma and Fusion Research. 2013;**8**:1402058

[27] Kobayashi M et al. Impact of resonant magnetic perturbation field on impurity radiation, divertor footprint, and core plasma transport in attached and detached plasmas in LHD. Nuclear Fusion. https://doi.org/10.1088/1741-4326/ab26e6

[28] Sudo S et al. Scalings of energy confinement and density limit in stellarator/heliotron devices. Nuclear Fusion. 1990;**30**:11. DOI: 10.1088/0029-5515/30/1/002

[29] Feng Y et al. Physics of the geometry-related detachment stability in W7-AS. Nuclear Fusion. 2005;**45**:89. DOI: 10.1088/0029-5515/45/2/003

[30] Pedersen TS et al. First divertor physics studies in wendelstein 7-X. Nuclear Fusion

[31] Masuzaki S et al. Effects of drifts on divertor plasma transport in LHD. Nuclear Materials and Energy. 2019;**18**:281. DOI: 10.1016/j.nme.2019.01.009

[32] Kobayashi M et al. Detachment stabilization with n/m = 1/1 resonant magnetic perturbation field applied to the stochastic magnetic boundary of the large helical device. Physics of Plasmas. 2010;**17**:056111. DOI: 10.1063/1.3368681

[33] Yokoyama M et al. Extended capability of the integrated transport analysis suite, TASK3D-a, for LHD experiment. Nuclear Fusion. 2017;**57**: 126016. DOI: 10.1088/1741-4326/aa800a

[34] Rechester AB, Rosenbluth MN. Electron heat transport in a tokamak with destroyed magnetic surfaces. Physical Review Letters. 1978;**40**:38. DOI: 10.1103/PhysRevLett.40.38

[35] Tokar MZ. On transport, in particular of impurities, in a stochastic magnetic field. Physics of Plasmas. 1999; **6**:2808. DOI: 10.1063/1.873238

[36] Prigogine I. Introduction to Thermodynamics of Irreversible Processes. 2nd ed. New York: Interscience; 1961

[37] Loarte A, Monk RD, Kukushkin AS, Righi E, Campbell DJ, Conway GD, et al. Self-sustained divertor plasma oscillations in the JET tokamak. Physical Review Letters. 1999;**83**:3657-3660

[38] Krasheninnikov SI, Kukushkin AS, Pistunovich VI, Pozharov VA. Self-sustained oscillations in the divertor plasma. Nuclear Fusion. 1987;**27**: 1805-1816

[39] Nedospasov AV, Tokar MZ, Vasin NL. Plasma recycling and MARFE phenomenon in a tokamak. Contributions to Plasma Physics. 1988; **28**:453-458

[40] Tokar MZ. Self-sustained oscillations in a plasma-wall system with strongly inhomogeneous diffusion of charged particles. Physical Review Letters. 2005;**95**:2650029. DOI: 10.1103/95.265002

[41] Tokar MZ. On threshold of radial detachment in tokamaks. Physics of Plasmas. 2000;**7**:2432-2438. DOI: 10.1063/1.874082

[42] Tokar MZ. Modelling of detachment in a limiter tokamak as a nonlinear phenomenon caused by impurity radiation. Plasma Physics and Controlled Fusion. 1994;**36**:1819-1843